

**AFM STUDIES ON FRACTURED SURFACES OF AF1410
STEEL AND AA7075-T6 ALUMINUM ALLOY**

By

Nairobi Bibiana Duque Rojas

A thesis submitted in partial fulfillment of the requirements for the degree of

MASTER OF SCIENCE

in

MECHANICAL ENGINEERING

UNIVERSITY OF PUERTO RICO

MAYAGÜEZ CAMPUS

2006

Approved by:

O. Marcelo Suárez, Ph.D.
President, Graduate Committee

Date

Paul Sundaram, Ph.D.
Member, Graduate Committee

Date

Néstor Pérez, Ph.D.
Member, Graduate Committee

Date

Oscar J. Perales, Ph.D.
Representative of Graduate Studies

Date

Paul Sundaram, PhD
Chairperson of the Department

Date

Abstract

In the present research, atomic force microscopy (AFM) was used to characterize fracture surfaces of the AF1410, ultra high strength steel, and a high strength AA7075-T6 aluminum alloy. Both materials are used by the U.S. Navy in aircraft parts. The implementation of a reliable qualitative and quantitatively technique that could reveal three-dimensional characteristics of the material fracture topography and the study of roughness parameters was necessary to explain the fracture surfaces (nano-fractography). Compact tension specimens made of AF1410 steel and AA7075-T6 alloy were exposed to different conditions at fatigue and impact-fatigue testing respectively. The bottom half of the fractured fatigued samples in the AF1410 steel and both of the impact fatigued sample for the aluminum alloy were used for AFM observations. The surface roughness was a parameter that aided to quantify the surface texture of the steel sample. Using AFM software, six roughness parameters were calculated over a determined area: the roughness average (S_a), the mean value (S_m), the root mean square (S_q), the valley value (S_v), the peak value (S_p), and the range between the peak and the valley value ($S_y=S_p-S_v$). The crack growth in fatigue testing of the AF1410 steel was analyzed in air and under 1, and 3.5% saline solutions. In the analyzed areas, the results indicated that decreasing NaCl concentration significantly enhanced the roughness average (S_a) in the crack growth direction due to an aggressive process of metal dissolution. When the material was tested at low frequencies and under low sodium chloride concentration, a much higher roughness average was obtained compared to the 3.5 % NaCl condition. With the AA7075-T6 alloy, grains orientation effect was analyzed using two specimens. In this work different crack propagation rates were found on the fracture surfaces, both for the longitudinal and for the transversal specimen.

Resumen

En el presente proyecto se utilizó un microscopio de fuerza atómica (AFM) para caracterizar las superficies de fractura del AF1410, un acero de altísima resistencia, y una aleación de aluminio AA7075-T6. Ambos materiales son usados por la marina de los Estados Unidos en partes de aviones. Para este fin, fue necesaria la implementación de una técnica especializada y confiable cualitativa y cuantitativamente que pudiera revelar características en tres dimensiones de la topografía del material; además el estudio de otros parámetros que explicaran las superficies de fractura (nano-fractografía). Especímenes compactos del acero AF1410 y de la aleación de aluminio AA7075-T6, fueron expuestos a diferentes condiciones al ensayo de fatiga e impacto-fatiga respectivamente. Para realizar las observaciones con el AFM se utilizaron las partes de abajo de las muestras fatigadas en el acero AF1410 y de ambas partes de la muestra ensayada en impacto-fatiga para la aleación de aluminio. La rugosidad de la superficie fue un parámetro que ayudó a cuantificar la textura de la superficie del acero. Utilizando el software del AFM, fueron calculados seis parámetros de rugosidad sobre un área determinada, los cuales fueron: rugosidad promedio (S_a), valor medio de la rugosidad (S_m), raíz cuadrada de la rugosidad (S_q), valor valle o mas profundo (S_v), valor del pico más alto (S_p) y rango entre pico-valle ($S_y=S_p-S_v$). El crecimiento de grieta en el ensayo de fatiga del acero AF1410 fue realizado en condiciones de laboratorio y en soluciones salinas de 1 y 3.5%. En las áreas analizadas, los resultados indicaron que una disminución en la concentración del NaCl aumentó significativamente la rugosidad promedio (S_a) en la dirección del crecimiento de la grieta debido a un proceso agresivo de disolución del metal. Cuando el material fue ensayado a baja frecuencia y con baja concentración de cloruro de sodio se halló una rugosidad promedio mucho mas alta comparada con la del espécimen sometido a condiciones de 3.5% NaCl. Con la aleación AA7075-T6, el efecto de la orientación de los granos en la aleación fue analizado utilizando dos especímenes. En este trabajo fueron halladas diferentes velocidades de propagación de grietas sobre las superficies fracturadas, tanto para el espécimen longitudinal como para el transversal.

This thesis is dedicated to my Father

Acknowledgments

I would like to express my gratitude to my advisor Dr. O. Marcelo Suárez.

Thanks to my friend Andrés F. Valencia and Orlando Cumdumi for the support received in the Matlab's[®] file.

Thanks to Juan G. Ramírez for his guidance in the fractals part.

Thanks to Mark Flowers for his support in the use of the AFM during this investigation.

The gratitude is also extended to the members of the committee: Dr. Oscar Perales, Dr. Paul Sundaram, and Dr. Néstor Pérez for their outlook.

This research was financed through the U.S. Navy project “Life prediction methodology for landing gears U.S. Navy” – ONR (Office of Naval Research) award number 000140310540.

Table of Contents

Abstract	ii
Resumen	iii
Acknowledgments	v
Table of Contents	vi
List of Figures	viii
List of Tables.....	x
List of Tables.....	x
1 INTRODUCTION	1
<i>1.1 Justification.....</i>	<i>1</i>
<i>1.2 Objectives.....</i>	<i>3</i>
2 ROUGHNESS AND FRACTAL ANALYSIS ON AF1410 STEEL FRACTURE SURFACES BY AFM	4
<i>2.1 AF1410 ultrahigh strength steel background.....</i>	<i>6</i>
<i>2.2 Background of fracture analysis using AFM</i>	<i>10</i>
<i>2.3 Methodology, equipment used and experimental procedure.....</i>	<i>11</i>
2.3.1 Sample preparation for experimental fatigue testing.....	11
2.3.2 Sample preparation for AFM observations	13
<i>2.4 Experimental setup.....</i>	<i>14</i>
<i>2.5 Roughness parameters</i>	<i>15</i>
2.5.1 Surface roughness calculations	15
2.5.2 Analysis of roughness parameters on AFM calibration grid	17
2.5.3 Roughness parameters on the fracture samples of the AF1410 steel	19
2.5.4 Results and Discussion.....	20
2.5.5 Roughness changes and crack growth propagation.....	24
<i>2.6 Fractals in fractured surfaces.....</i>	<i>26</i>

2.6.1	Fractal background.....	27
2.6.2	Hurst exponent	30
2.6.3	Results and Analysis	31
3	HYDROGEN EMBRITTLEMENT EFFECT ON AF1410 STEEL	37
3.1	<i>Experimental setup</i>	37
3.2	<i>Analysis of results</i>	39
4	GRAIN ORIENTATION IN ALUMINUM ALLOY 7075-T6 FRACTURED IN FATIGUE TESTING	46
4.1	<i>Influence of grain orientation in the fracture behavior of Al-alloy</i>	46
4.2	<i>Methodology and experimental procedure</i>	48
4.2.1	Aluminum alloy characteristics.....	48
4.2.2	Sample preparation and experimental fatigue testing.....	50
4.3	<i>Results and Discussion</i>	50
5	CONCLUSIONS	59
6	References.....	60
	APPENDIX	64

List of Figures

Figure 2.1 Schematic diagram of atomic force microscope [13].....	5
Figure 2.2 Schematic AFM contact mode probe [16]	5
Figure 2.3 Comparison between ultrahigh strength steels [19]	7
Figure 2.4 Fracture toughness [19].....	8
Figure 2.5 Mechanical grinding and polishing machine	12
Figure 2.6 MTS uniaxial testing machine and assembly of the COD gage.....	12
Figure 2.7 Sample preparation procedure.....	13
Figure 2.8 AFM EasyScan [®] used in this research	15
Figure 2.9 Roughness average [26].....	16
Figure 2.10 AFM image of silicon oxide blocks on a silicon substrate using SPIP [™]	18
Figure 2.11 AFM image of silicon oxide squares of a silicon substrate using Matlab [®]	18
Figure 2.12 AFM images in contact mode over the crack growth direction 1 mm after precrack line in AF1410 steel. Left to right: specimen in air and saline solution (1% NaCl) in scanning area of 2519.6 μm^2	19
Figure 2.13 Scheme of the fractured specimen indicating the 8 different distances from the precrack	20
Figure 2.14 Roughness average vs. distance from precrack line in AF1410 steel. a) 1% NaCl at 1 and 0.5 Hz; b) 3.5% NaCl at 1 and 0.5 Hz; c) 1% NaCl and 3.5% NaCl at 1 Hz; d) 1% NaCl and 3.5% NaCl at 0.5 Hz; e) Cadmium plated steel and 1% NaCl at 1 Hz; f) Cadmium plated steel and 3.5% NaCl at 1 Hz.....	22
Figure 2.15 Average results of CFCG shown for AF1410 specimens	24
Figure 2.16 Growth of the interface with time for the BD model [14].....	28
Figure 2.17 Longitudinal profile corresponding to the crack growth sense	30
Figure 2.18 Hurst exponent in AF1410 at air conditions at 3 Hz in an area of 2519.6 μm^2	32
Figure 2.19 Hurst exponent in AF1410 using a 50 μm scan range	33
Figure 2.20 Roughness and Hurst exponent dependence at frequency and NaCl concentration.....	35
Figure 3.1 Electrochemical cell for hydrogen permeation	38
Figure 3.2 Specimen input hydrogen face (roughness average 0.223 μm), output hydrogen face (roughness average 0.0879 μm)	39
Figure 3.3 AFM images over crack way in the AF 1410 steel. a) H-charged side; b) non-affected region ..	40
Figure 3.4 Crack growth rates as a function of crack path	41
Figure 3.5 Scanning electron microscope Image of a hydrogen charged specimen of AF1410. a) Hydrogen non-affected zone (roughness average 0.71 μm), b) Hydrogen affected zone (roughness average 1.75 μm)	42
Figure 3.6 Fracture surface specimen (fast crack growth velocity).....	43

Figure 3.7 Fracture surface specimen (slow crack growth velocity).....	44
Figure 4.1 <i>a</i>) Image taken in contact mode with AFM at a longitudinal section parallel to the rolled surface revealing a microstructure characteristic of AA 7075-T6. <i>b</i>) Longitudinal and transversal grain orientation	49
Figure 4.2 AA7075-T6 microstructure showing irregular grains	50
Figure 4.3 Optical micrograph of rolled sample revealing a microstructure characteristic of AA7075-T6 aluminum alloy	51
Figure 4.4 Transversal grain orientation in 2D, AFM image	52
Figure 4.5 Transversal grain orientation in 3D, AFM image	52
Figure 4.6 Transversal sample (T) after tested in fatigue-impact.....	53
Figure 4.7 Microcracks perpendicular at crack growth direction (arrow point towards them)	54
Figure 4.8 Longitudinal sample (L) after tested in fatigue-impact.....	54
Figure 4.9 Irregular fracture in L orientation	56
Figure 4.10 Fatigue striations on the fracture surface of AL7075-T6 in crack front direction.....	57
Figure 4.11 Striation profile in the crack growth direction	57
Figure 4.12 AA 7075-T6 grains showed in T-orientation	58
Figure 4.13 AA 7075-T6 grains showed in L-orientation	58

List of Tables

Table 2.1 Nominal chemical composition of AF1410 steel [21].....	9
Table 2.2 Mechanical properties of AF1410 steel [21]	10
Table 2.3 Roughness parameters of silicon grid.....	19
Table 2.4 Mean Hurst exponent in AF1410 samples	34
Table 4.1 AA7075-T6 chemical composition	48
Table 4.2 AA 7075-T6 alloy mechanical properties	49

1 INTRODUCTION

During maintenance inspections in aircrafts, engineers find small cracks in structural components that eventually can cause catastrophic failures in the materials. These failures are produced by metal fatigue, having as result fractures in the material. Consequently, it is necessary to identify the formation causes of these cracks through the fracture surfaces characterization of the broken parts. Therefore, the implementation of a specialized technique is necessary to reveal three dimensional features and roughness parameters on the material surface. It can be correlated with test conditions and crack growth propagation process.

In the study of aerospace structural materials the use of the atomic force microscope (AFM) is essential to investigate materials of commercial and military types due to the high resolution and quantitative information about surface that it offers. In this research, fracture surfaces of two materials of use to the military will be analyzed.

1.1 Justification

This research investigates a means to study the fractured surfaces of two materials: the AF1410 steel and the AA7075-T6 alloy using AFM and other optical techniques. These materials are utilized by the United States Navy in critical military F18 aircraft parts. AF1410 steel is used in arresting shanks and landing gears, due to the high toughness, high ultimate tensile strength, and appropriate corrosion resistance of this steel. AA7075-T6 is widely used in aircraft structural longeron and frame elements. However, marine environment combined with cyclic loads eventually affect the life of these structural components. As a consequence, there exists a need to carry out a systematic research of this ultra-high strength steel by means of atomic force microscopy (AFM) coupled with fatigue test data.

The fracture surfaces of many metallic materials as a result of fatigue have been studied by many researches by means of AFM such as: α -brass, high strength low alloy steel AISI 4135, austenitic stainless steel, 7xxx series aluminum alloys, 2017-T4 alloy, 2017-T351 aluminum alloy, silver single crystals, Ti₃Al – based alloy, Al-Li alloy, AISI 4340 steel, OFHC Cu, 13-8 PH stainless steel, and Ti-15-3 alloy reinforced with carbides [1]. Nevertheless, for the first time an analysis was performed on the fractured surface of the AF1410 using the AFM technique since it is a material of military use. Even though, it has an extremely high strength, it was possible to use this microscopy technique to try to correlate roughness parameters with the advanced crack growth.

On the fracture surface, during fatigue crack growth (stage II) some materials show fatigue striations [11]. Depending on the stress intensity factor range (ΔK) and the crack growth rate there is a correlation between da/dN and the striation spacing. In the AF1410 ultrahigh strength steel, the correspondence between da/dN and striation spacing was not observed in the AFM images. Also, not all materials exhibit striation formation during stage II crack growth. Striations are more commonly observed in ductile materials such as aluminum alloys and less frequently observed in steels. Regularly, striations are difficult to find in high-strength materials [11]. Striations were present in AA7075-T6 alloy, where its formation was influenced by the alloy content and crack growth rate.

In the aluminum alloy 2017-T4 (UTS=435 MPa), type 304 stainless steel (UTS=650 MPa), high Mn steel (UTS=947 MPa) [4], nickel superalloy N18 [12], fatigue striations were revealed in AFM images, since these materials are ductile and possess lower toughness compared to AF1410 steel (UTS=1800 MPa).

Another new study was done on the crack front growth of the AF1410 fractured surfaces using the AFM images and the variable bandwidth method to find Hurst exponent. A 0.5 value means that fatigue load testing was done under a quasi-static regime using small scale lengths and slow crack propagation. This is what was revealed on the material surface.

Each chapter in the thesis was structured in independent form analyzing the fracture surface of two military materials (AF1410 steel and aluminum alloy AA7075-

T6) by means of AFM. To implement this plan this thesis has been organized as follows. Chapter one, is an introduction to the materials studied in this research. A study of roughness parameters and a fractal analysis in AF1410 steel is described in the second chapter. In chapter three the fracture analysis of hydrogen embrittlement effects on AF1410 steel is shown. In chapter four, the fractured surfaces of aluminum alloy AA7075-T6 are studied. Finally, the overall conclusions are presented in chapter five.

1.2 Objectives

The main goal of the present research is to study fatigue fracture surfaces using an AFM. The specific objectives are:

- Analyze the relevance of the roughness on the AF1410 fracture surfaces in the study of fatigue specimens using AFM.
- Perform a quantitative analysis of the roughness exponent ζ on the AF1410 steel, using the profiles generated by AFM images through the variable bandwidth method.
- Understand the effect of hydrogen on the mechanical properties of AF1410 steel.
- Characterize the AA7075-T6 aluminum alloy fracture surfaces using optical, stereoscopic and AFM techniques.

2 ROUGHNESS AND FRACTAL ANALYSIS ON AF1410 STEEL FRACTURE SURFACES BY AFM

For qualitative analysis in fractography, SEM (scanning electron microscopy) and stereoscopic techniques are widely used but are limited by quantitative measurements on the surface such as, roughness and striations on fractured surface. Therefore, the implementation of a reliable and specialized qualitative and quantitative technique that can reveal the three-dimensional characteristics of the surface and the study of related parameters is necessary. At the microscopic and submicroscopic scales such possibility is now offered by atomic force microscopy (AFM).

Figure 2.1 shows the AFM scheme, which consists of a cantilever and an integrated tip. While the tip makes contact with the sample surface, a laser beam, focused on the back of the cantilever, reflects onto a quadrant photodetector. The deflection in cantilever due to applied normal and lateral forces can be measured by monitoring the variation in the photodetector signal. This allows the force detection in the nano-Newton to pico-Newton (10^{-9} to 10^{-12} N) regime [13].

The principles of operation of an AFM are very simple: an extremely, usually atomically, sharp tip made of Si or Si_3N_4 is micro machined at the end of a flexible cantilever. The sensors used in this study were of silicon. It is then positioned in close proximity of the sample surface, where the cantilever is bent by the atomic force between the tip and sample surface [14]. The tip geometry that was used during this work is shown in Figure 2.2. This tip is a contact mode nano-sensor, with a tip radius of 7 – 10 nm and 30nm aluminum reflex coating on cantilever side that improves reflectivity.

The scanning tunneling microscope (STM) was developed by Gerd Binnig and Heinrich Rohrer in the early 80's at the IBM research laboratory in Ruschlikon,

Switzerland. For this revolutionary innovation Binnig and Rohrer were awarded the Nobel prize in physics of 1986. However, the STM technique was restricted to electrically conducting surfaces. A further development of the STM called the atomic force microscope (AFM) was developed by Gerd Binnig, Calvin Quate and Christoph Gerber. The AFM extended the abilities of the STM by including the analysis of insulating material. Both the AFM and the STM techniques work without optical focusing elements [14].

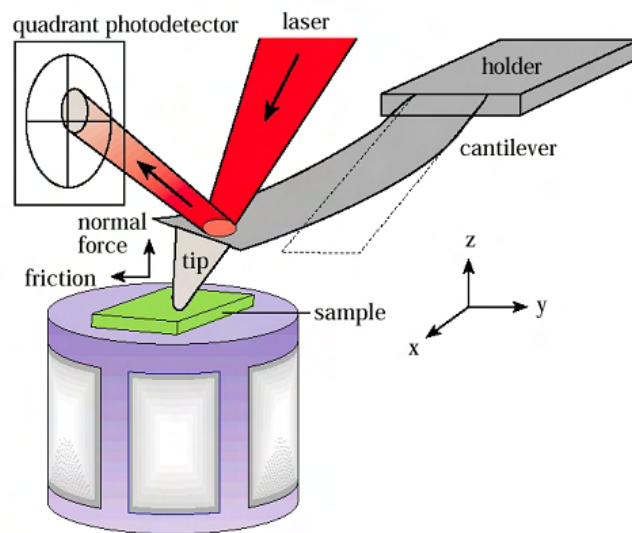


Figure 2.1 Schematic diagram of atomic force microscope [13]



Figure 2.2 Schematic AFM contact mode probe [16]

2.1 AF1410 ultrahigh strength steel background

Ultrahigh strength steels are a group of steels which have been used in airplanes and missiles where high values of the strength/weight ratio are needed. These steels have been developed in a number of different ways, using different compositions [17]. Steels with a yield strength > 200 ksi [18] are considered as ultra-high strength steels. Ultrahigh strength steels include a number of families of steels. In order to understand these alloys authors divide them into two categories: medium-carbon low-alloy/medium-alloy-air-hardening steels and high fracture toughness steels. In general, high fracture toughness steels present the following characteristics [19]:

- Novel alloys (ongoing alloy development)
- High fracture toughness (K_{IC} 100 MPa \sqrt{m} or higher)
- A high cost
- Microstructure-lath martensite, aged
- Less susceptible to hydrogen embrittlement
- Better resistance to stress corrosion cracking and higher fatigue life

Therefore, the AF1410 steel with ultra high strength of 261 ksi, high fracture toughness, high price and high fatigue life, is considered an ultrahigh strength steel into high fracture toughness steels category. Figure 2.3 illustrates yield and tensile strength comparisons between steels with high strength. The AF1410 is presented into others ultra high strength alloys.

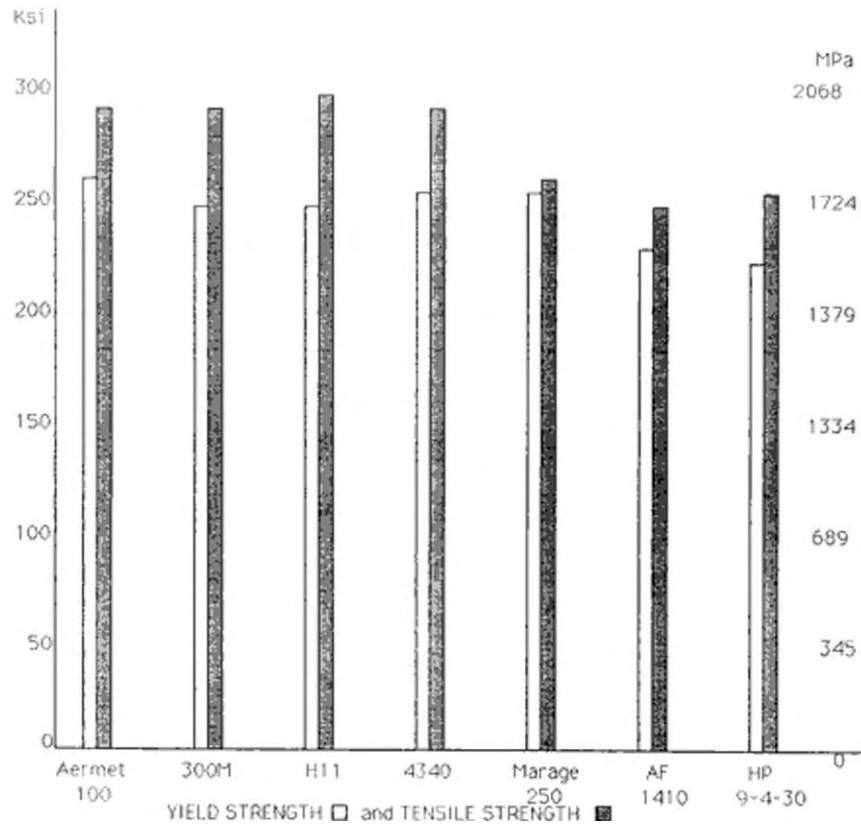


Figure 2.3 Comparison between ultrahigh strength steels [19]

The U.S. Navy sponsored a program to produce advanced submarine hull steels developing a series of Fe-Ni-Co low-carbon steels. These alloys exhibited great ability to absorb energy up to fracture [20]. Air Force sponsored additional development efforts, which resulted in AF1410 steel. This alloy contains higher cobalt and carbon alloying elements, resulting in an ultimate tensile strength of 235 ksi. The critical stress intensity factor for mode I crack opening (K_{IC}) was maintained at $140 \text{ ksi}\sqrt{\text{in}}$ with high stress corrosion cracking resistance. The microstructure is Fe-Ni lath martensite. Melting process requires that impurity elements remain low to insure good fracture toughness.

Figure 2.4 displays fracture toughness of various ultrahigh strength materials, where AF1410 steel toughness is highlighted over the other materials [19].

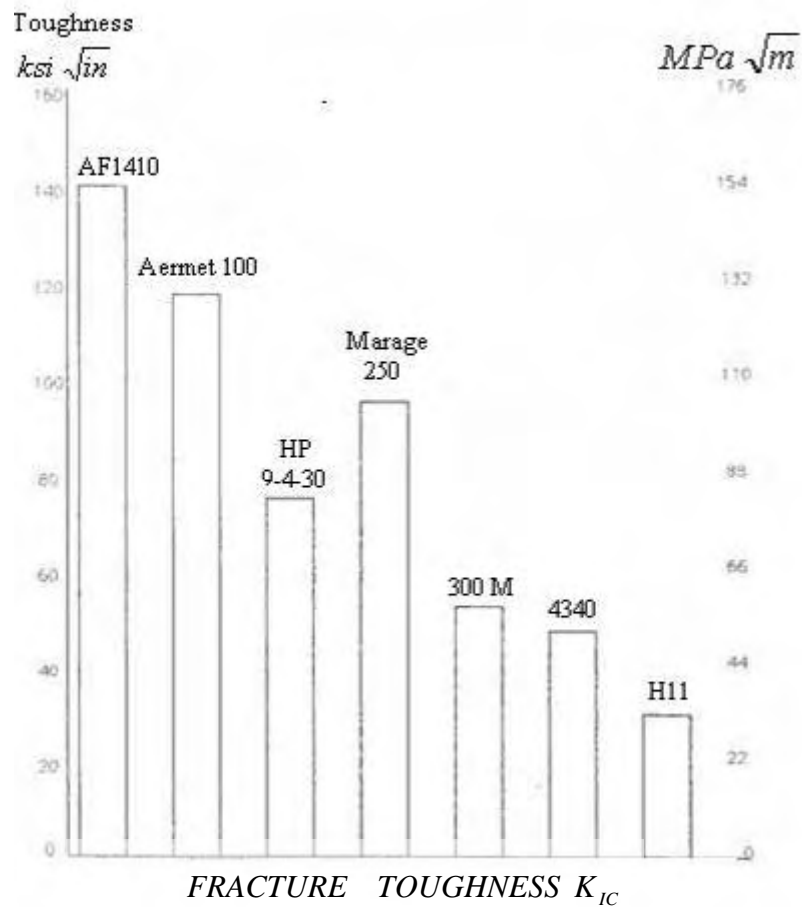


Figure 2.4 Fracture toughness [19]

The chemical composition, mechanical properties and heat treatment of AF1410 steel, as determined by Carpenter Technology Corp. are indicated in Table 2.1 and Table 2.2 [21]. AF1410 samples were heat-treated under the following conditions:

- Heat treatment atmosphere: air, combustion products, argon, helium use a dew point less than $-40\text{ }^{\circ}\text{C}$
- Austenitizing at $857\text{ }^{\circ}\text{C}$, for 1-2 hours
- Oil quenching at temperatures between $24\text{ }^{\circ}\text{C}$ and $60\text{ }^{\circ}\text{C}$
- Within one hour of quenching, refrigerate at $-73\text{ }^{\circ}\text{C}$ for at least 1 hour

- Air warm to room temperature
- Age hardening at 510 °C for 5 to 8 hours
- Air cool to room temperature
- Secondary hardening at 510 °C for 4 to 7 hours

The retardation of dislocation recovery imparted by the cobalt allows an unusually high dislocation density to remain during secondary hardening, which is a result of the precipitation on dislocations of a low volume fraction of finely-dispersed metastable M_2C (principally Mo_2C) carbides during high temperature tempering (*Chang, et al., 1985; Grujicic, 1989; Haidemenopoulos, 1988; Lee, 1989* cited from Jemian, 1990). The M_2C distribution exhibits sufficient coarsening resistance to maintain the alloy strength and so the M_3C (cementite) platelets, which limit the fracture toughness, can be re-solutioned by slight overaging [22].

The purpose of the heat treatment is the precipitation of extremely fine alloy carbides containing chromium and molybdenum, which develop strength and toughness properties.

Table 2.1 Nominal chemical composition of AF1410 steel [21]

Component	wt%
<u>C</u>	<u>0.16</u>
<u>Co</u>	<u>13.8</u>
<u>Ni</u>	<u>10.00</u>
<u>Cr</u>	<u>2.00</u>
<u>Mo</u>	<u>1.00</u>
<u>Mn</u>	<u>0.16</u>
<i>Ti</i>	- 0.015
<i>Al</i>	- 0.015
<i>S</i>	- 0.005
<i>P</i>	- 0.008
<i>O</i>	- 0.002
<i>N</i>	- 0.0015

Table 2.2 Mechanical properties of AF1410 steel [21]

Properties	Minimum
UTS (GPa)	1.8
Yield strength 0.2% offset (MPa)	1478
Elongation (%)	12
Reduction area (%)	60
Fracture Toughness K_{IC} (MPa · m ^{1/2})	130
Hardness HRC	47 to 50

2.2 Background of fracture analysis using AFM

High strength steels can be sensitive to aggressive environment, and the subsequently induced degradation including stress corrosion cracking (SCC) shortens the lifetime of components significantly [23]. As a consequence, there exists a need for a systematic study of this ultra-high strength steel by means of AFM coupled with fatigue test results. Environmental effects reduce the lifetime of steel components under cyclic loading conditions, i.e. corrosion-fatigue processes. Local corrosion can produce stress concentration whereas a general corrosion type can cause a dimensional reduction by loss of material, so that cracking by fatigue appears in that corroded region, which can be analyzed with the AFM.

Recently in fractography, the AFM has become a necessary tool to determine topography features on fracture surfaces. Komai *et al.* [23] worked on in-situ visualization using AFM. The nanoscopic initiation and growth mechanisms of localized corrosion crack and stress corrosion in austenitic stainless steel and 7XXX series aluminum alloys were analyzed. They determine that most damage issues in machines and structures are caused by environmentally induced material degradation in an operating environment, including corrosion fatigue and stress corrosion cracking. In order to clarify the fracture and damage mechanisms of this environmentally induced material degradation, high magnification observation of damage initiation and growth processes are deemed as necessary. This investigation proved that an AFM is capable of performing *in-situ* nanoscopic visualization of the initiation and progress of localized corrosion

damages as well as stress corrosion cracking in austenitic stainless steels and aluminum alloys.

The AFM is ideal for quantitatively measuring the surface roughness at the nano-scale and for visualizing the surface nano-texture of many types of materials. Advantages of the AFM for such applications are derived from the fact that the AFM is nondestructive and that it has a high three dimensional spatial resolution [24].

2.3 Methodology, equipment used and experimental procedure

2.3.1 Sample preparation for experimental fatigue testing

The AF1410 steel specimens were cut from plates by electric-arc discharge machining technique (EDM). Afterwards, they were machined prior to fatigue testing. The research was conducted at 25 °C on 1.80 inches x 1.85 inches x 1/8 inches compact tension (CT) specimens of AF1410 steel. All specimens were pre-cracked according to the ASTM E399-95 method [28]. Each specimen was mechanically ground with 240, 320, 400, 600 and 800 grit papers in an automatic polishing machine Buehler Ecomet 3 (Figure 2.5); the last step in the polishing procedure included the use a 0.05 μm silica suspension on a Chemomet Buehler cloth. This process was used in order to obtain bright lateral surfaces to observe the crack growth while the fatigue testing was being carried out. Then the sample was fatigued.

The crack growth data for a CT steel specimen was obtained by fatigue in a 22,000 lbs MTS uniaxial testing machine, coupled with a liquid container used for testing specimens with the crack tip fully immersed in an aqueous solution. The unit, furnished with Instron electronics, allowed the required COD (crack opening displacement) control testing conditions, as Figure 2.6 shows. Conventional crack growth tests were carried out on pre-cracked specimens under a maximum stress, $\sigma_{\text{max}}=1,620$ MPa, a stress ratio of $R=0.4$, $K_{\text{IC}}=21,518$ $\text{lb}\cdot\sqrt{\text{in}}$, frequency of 1 Hz (with sinusoidal loading) to complete 95,000 cycles [28]. Each test machine was interfaced with a computer system for continuous monitoring of fatigue load and crack growth.



Figure 2.5 Mechanical grinding and polishing machine

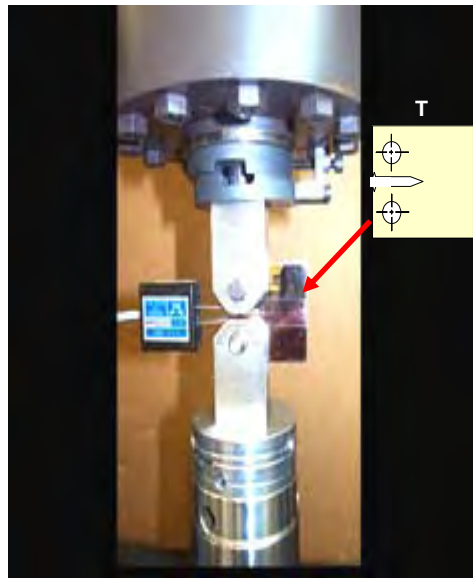


Figure 2.6 MTS uniaxial testing machine and assembly of the COD gage

2.3.2 Sample preparation for AFM observations

For AFM observations the bottom half of the fractured sample was used. For such process immediately after testing, the fractured sample was protected with wax paper. On applying heat with a hot air blower, the wax adhered to the sample surface, covering it and protecting it from the cutting machine cooling liquid, to avoid the oxidation of the material and the subsequent alteration of the topography.

Figure 2.7 displays the method used in this work. Finally, the specimens were cleaned in an ultrasonic cleaner for five minutes submerged in ethanol.

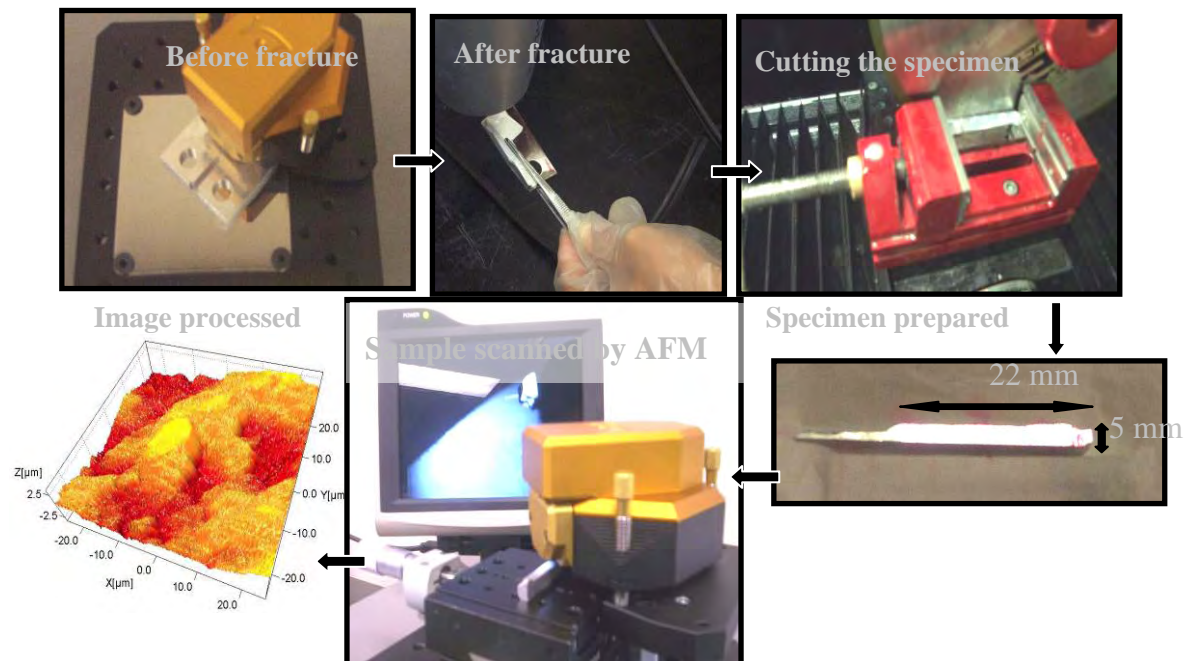


Figure 2.7 Sample preparation procedure

2.4 Experimental setup

For the observations, the fractured specimen was mounted on a special table under the AFM, which was operated under static force mode. Prior to any quantitative analysis via AFM, it was determined that the best operation conditions were attained with contact mode in the AFM. This is due to the fact that during the AFM scanning the cantilever tip crashed with fractured surface in many occasions caused by the irregularities on fatigued material surface. This static force acting on the cantilever was used to produce a topographic image of the sample. AFM images were generated with a z-range of 10 μm in a square area of 2,500 μm^2 at 8 different points located parallel to front crack line. The AFM unit used is presented in Figure 2.8.

In effect, our AFM unit generates 3-D images of a surface with high resolution (97.65nm/pixel). This capability facilitates the topographic study of a fracture surface (nano fractography) [2], so that microscopic fracture mechanisms can be determined. In particular, fatigue striations can be analyzed with this instrument [4] [12].

In the present research project AFM was used to characterize fracture surfaces and the results were correlated with fatigue tests conducted under crack-opening displacement (COD) conditions. To replicate the operating conditions of AF1410 parts in naval aircrafts, a marine environment was simulated using saline solutions with two different concentrations: 1% and 3.5% NaCl.

Compact tension specimens made of AF1410 steel were exposed to different conditions for fatigue testing. The specimens were tested in air (to set up a research baseline) and simulated marine environments, under at different loading frequencies (0.5 and 1 Hz). In addition AF1410 cadmium plated steel at 1 Hz was used to appreciate the effect of atomic hydrogen near to the AF1410 surface. The intention was that atomic hydrogen from the cadmium plate (above 300 ppm) would diffuse into the steel surface at an accelerating rate under fatigue stresses and migrate towards the crack tip doing brittle the AF1410.

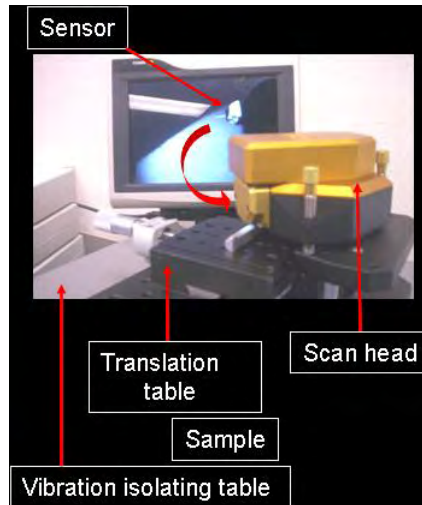


Figure 2.8 AFM EasyScan[®] used in this research

2.5 Roughness parameters

Some factors that can affect surface roughness values in the fractured surface are: surface topography, scanning area, time/line scanning parameter and distance after precrack line. Other authors point out that the two primary potential sources of error in using an AFM for measuring surface textures are the probe geometry and the length scale of the measurement [24]. Within the image used for the surface/area roughness calculation there must be an adequate sampling of the features resulting from the surface texture. As a result, it is possible to obtain different surface texture when the scan size is changed. This problem is avoided by using the same scan range size when surface roughness on several samples is to be compared.

2.5.1 Surface roughness calculations

Initially, roughness parameters were used for characterizing machined surfaces. Nowadays they are also used for characterizing all types of nano-structures [25]. Optimal characterization of surface texture is expressed with area roughness calculations that are made on the entire surface. Surface roughnesses calculations are comparable between different areas studied provided that 'x' and 'y' ranges are identical.

The AFM software allows the calculation of several roughness parameters over the measured area e.g. the roughness average (S_a); the mean value (S_m); the root mean square (S_q); the valley value (S_v); the peak value (S_p); and the range between the peak and the valley value ($S_y=S_p-S_v$). The average roughness is also known as arithmetic average (AA), center line average (CLA) or R_a [26]. This parameter is determined by the easyScan E-line software[®] (Equation 2.1) as the summation of the absolute value of the roughness profile height in z , over a predetermined area limited by x and y axes, above the total number of data as is shown in Figure 2.9. MN is the columns and rows product of matrix measuring of the AFM.

$$S_a = \frac{1}{MN} \sum_{k=0}^{M-1} \sum_{l=0}^{N-1} |z(x_k, y_l)| \quad \text{Equation 2.1}$$

S_a always takes the absolute values of the heights (non-negative numbers ≥ 0), on the scanned area. Then, the acquired average roughness value is bigger than the value obtained with the summation without absolute value (Equation 2.3). Additionally, if the material surface is almost flat (graphically the peak values are larger than the valley values) $S_a \cong S_q$.

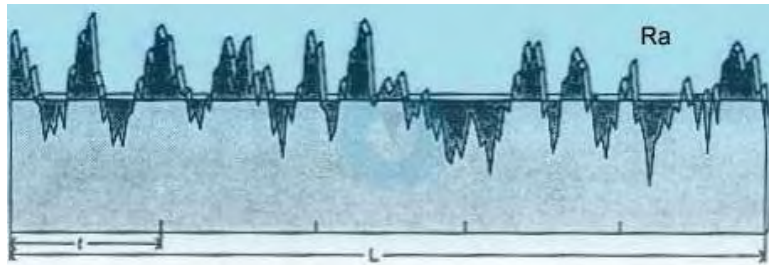


Figure 2.9 Roughness average [26]

The root mean square (rms) average roughness of a surface is calculated from the following summation of the roughness profile (Equation 2.2). This equation is the squared root of the mean squares of the roughness average.

$$Sq = \sqrt{\frac{1}{MN} \sum_{k=0}^{M-1} \sum_{l=0}^{N-1} (z(x_k, y_l))^2} \quad \text{Equation 2.2}$$

The mean value parameter (Sm) is defined by Equation 2.3:

$$Sm = \frac{1}{MN} \sum_{k=0}^{M-1} \sum_{l=0}^{N-1} z(x_k, y_l) \quad \text{Equation 2.3}$$

In equation 2.2 when the heights ($z(x_k, y_l)$) are elevated at the square, valley values of “z” are minimized, adding just a little amount to the total value of the summation. In contrary, peak values produce great values of Sq. Therefore, Sq is the highest between Sa and Sm parameters.

2.5.2 Analysis of roughness parameters on AFM calibration grid

Surface topography was analyzed by means of six roughness parameters delivered by the microscope software. In order to verify the correct functioning of the AFM a xyz calibration grid supplied with the microscope was used. However, non-standard roughness values were provided by the supplier. The grid was made using a standard silicon masking process that created silicon oxide squares on a silicon substrate. Figure 2.10 shows the topography obtained via scanning probe image processor software (SPIP™). Figure 2.11 shows the same grid plot using Matlab® software with colors scale. Taking the same area ($3047.3 \mu\text{m}^2$) in the silicon grid, as well as the z-range and doing the withdrawal and the tip approach toward the sample by means of the AFM, the six roughness parameters were evaluated three times (Table 2.3). The values obtained from Sa and Sq are given in Table 2.3. In the roughness values the only observed variability was in the third and fourth digits. Since the ‘Sy’ parameter is the difference between Sp and Sv, the variability of Sp affects heavily those Sy values. Therefore, Sp and Sy parameters were found too dubious to describe the topography of these fractured specimens.

For that reason, both roughness average and root mean square parameters were preferred to perform roughness comparisons in the fractured area in the AF1410 steel.

Additionally, Sv was useful in corrosion surface analysis in the AF1410. These preliminary tests corroborated that the AFM can be used in fractography with advantages over other conventional techniques such as SEM and optical microscopes.

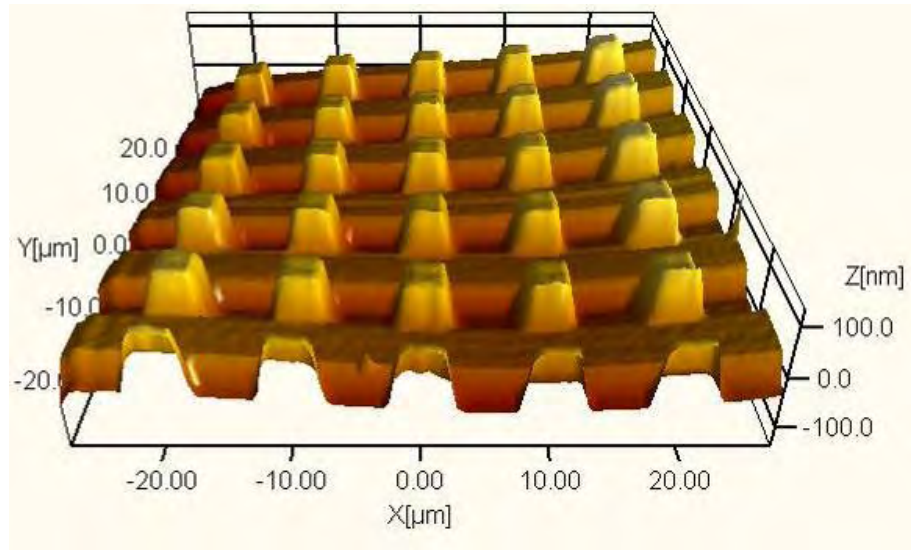


Figure 2.10 AFM image of silicon oxide blocks on a silicon substrate using SPIP™

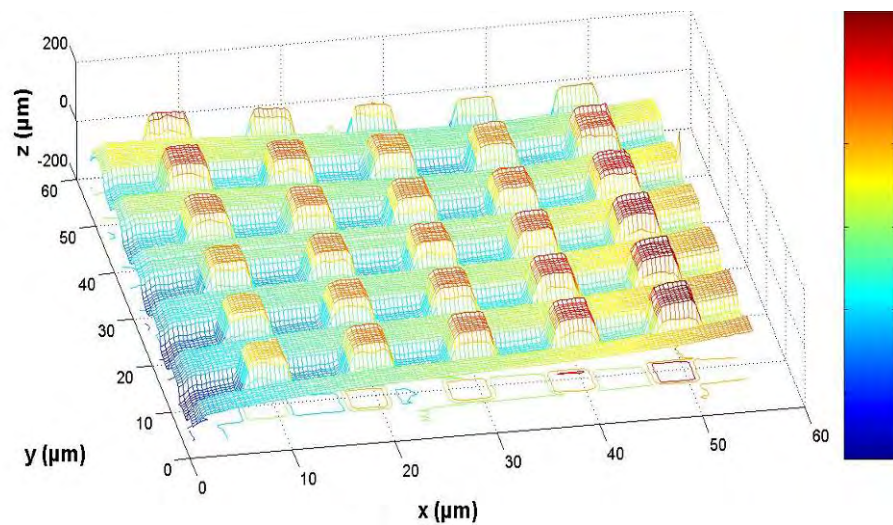


Figure 2.11 AFM image of silicon oxide squares of a silicon substrate using Matlab®

Table 2.3 Roughness parameters of silicon grid

Measurements, μm	1	2	3
Z-Range	0.6250	0.6250	0.6250
Sa	0.0291	0.0292	0.0287
Sq	0.0413	0.0414	0.0399
Sy	0.5140	0.5540	0.4630
Sp	0.3140	0.3140	0.3140
Sv	-0.2010	-0.2400	-0.149
Sm	0.0019	0.0012	0.00117

2.5.3 Roughness parameters on the fracture samples of the AF1410 steel

Employing the easyScan E-line software[®], used for the calibrated grid, the previously mentioned roughness parameters were determined for the AF1410 steel. These values were verified to determine if they could be used for the analysis of the fracture. Figure 2.12 illustrates the AF1410 steel fractures under two different environment conditions: air (research baseline) and 1% NaCl (saline solution) at 3 and 0.5 Hz of frequency respectively (stage II of the crack propagation).

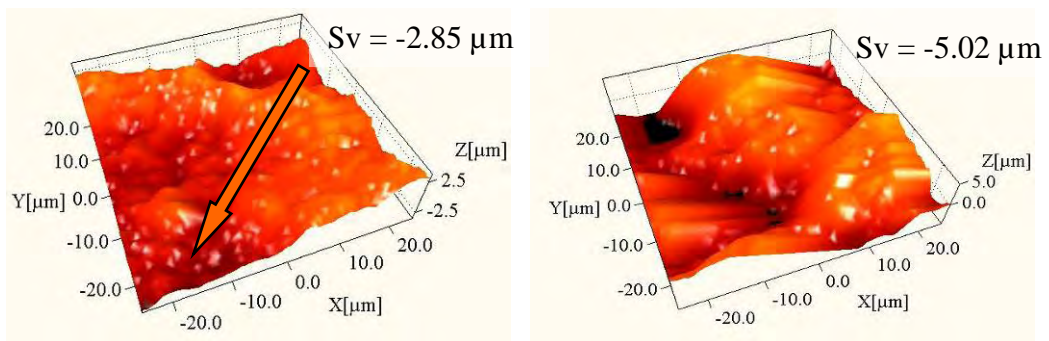


Figure 2.12 AFM images in contact mode over the crack growth direction 1 mm after precrack line in AF 1410 steel. Left to right: specimen in air and saline solution (1% NaCl) in scanning area of $2519.6 \mu\text{m}^2$

Schematically, Figure 2.13 shows the bottom part of AF1410 fractured sample with the 8 areas used in roughness analysis over the fracture surface.

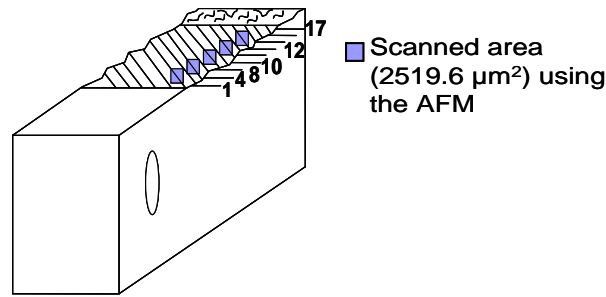
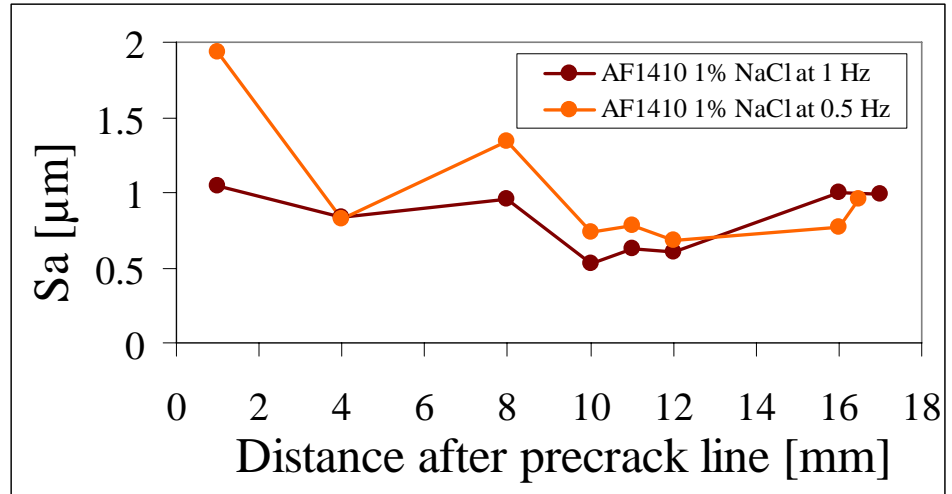


Figure 2.13 Scheme of the fractured specimen indicating the 8 different distances from the precrack

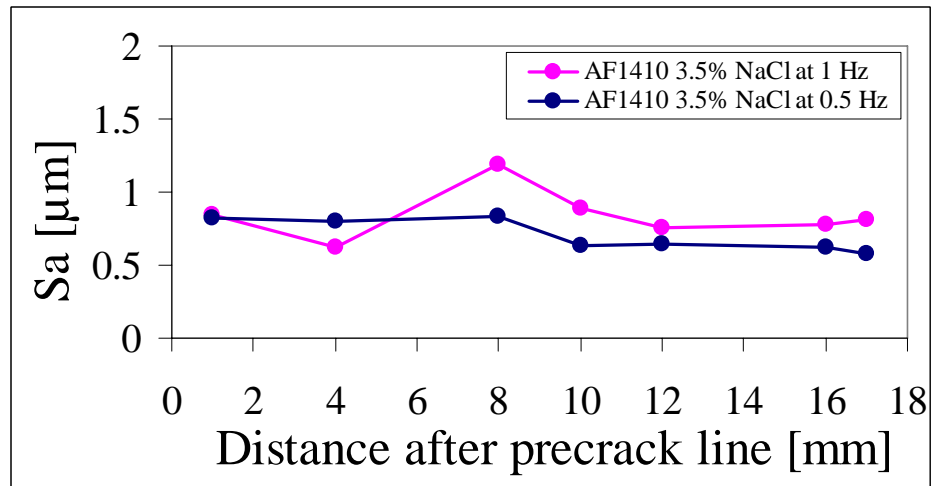
2.5.4 Results and Discussion

The roughness values include the finest (shortest wavelength) surface irregularities. The lowest value (S_v) for air and 1%NaCl specimens were $-2.85 \mu\text{m}$ and $-5.02 \mu\text{m}$ respectively as shown in Figure 2.12. The operating conditions that delivered well defined images of the materials mentioned before were the following: $20 \cdot 10^{-9}$ N of force and a frequency of 2 Hz; the cantilever spring constant was 0.20 ± 0.08 N/m and the scanning frequency was 0.5 s per line. The scanning was slow but a better reading of information was obtained. Although the scanning was slow-paced some particles of oxide stuck to the cantilever tip interrupting the reading. Figure 2.14 correlate the six parameters with the different distances from the precrack line to get clear evidence of the effect of an aggressive environment on the AF1410 fracture surface roughness measured in millimeters. The data used to plot the scanned areas of fracture surfaces in the AF1410 was: one AFM image that means one roughness value without repetition, for each distance after the precrack line. A scanned area by AFM is different from another one on the same surface, since the range is too small and it is impossible to obtain the first area scanned for a second time. Therefore, the plots did not have trend lines since each point was a fractured area.

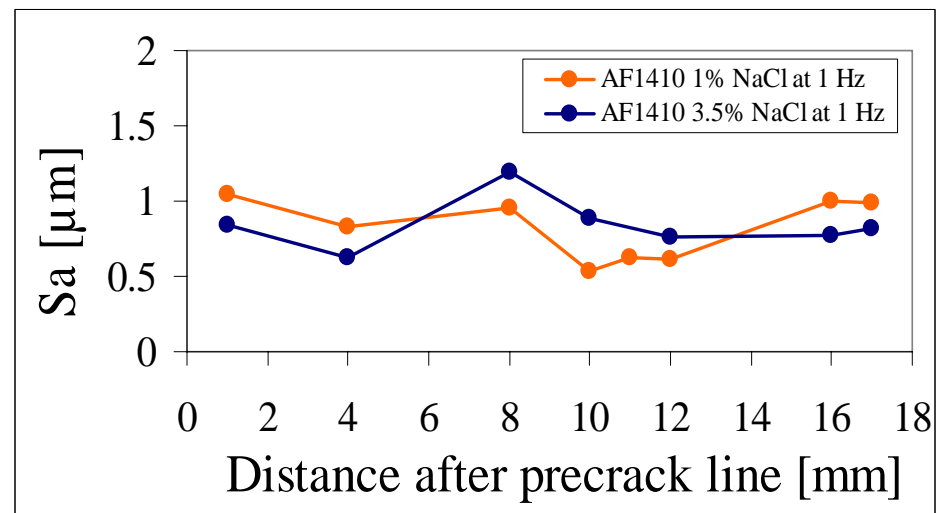
a)



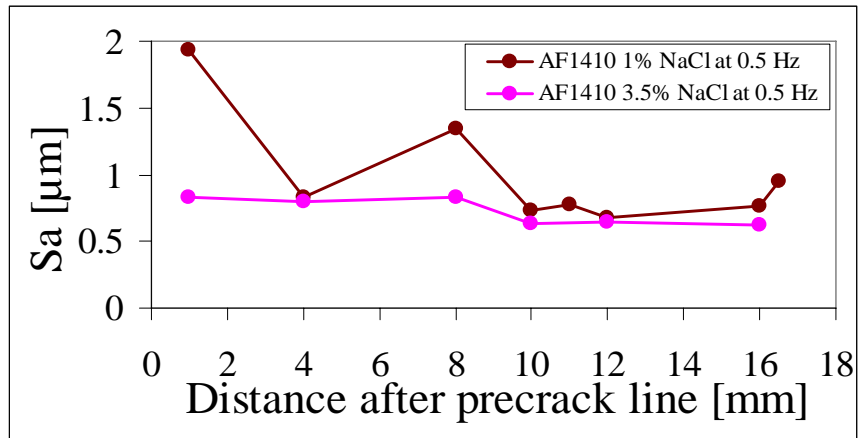
b)



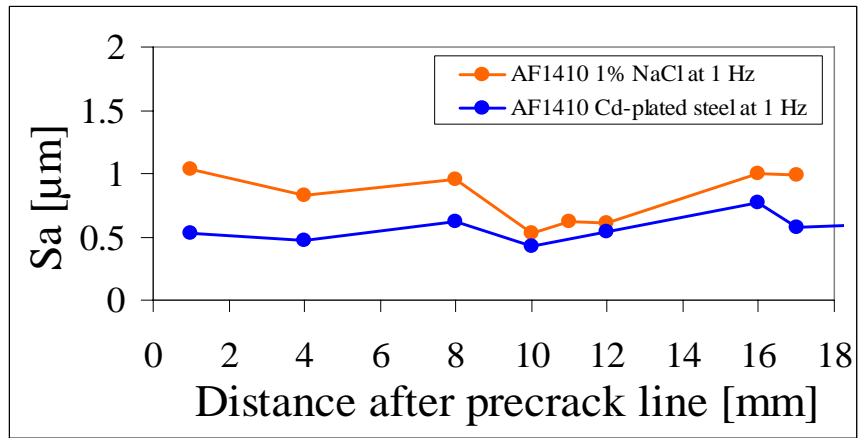
c)



d)



e)



f)

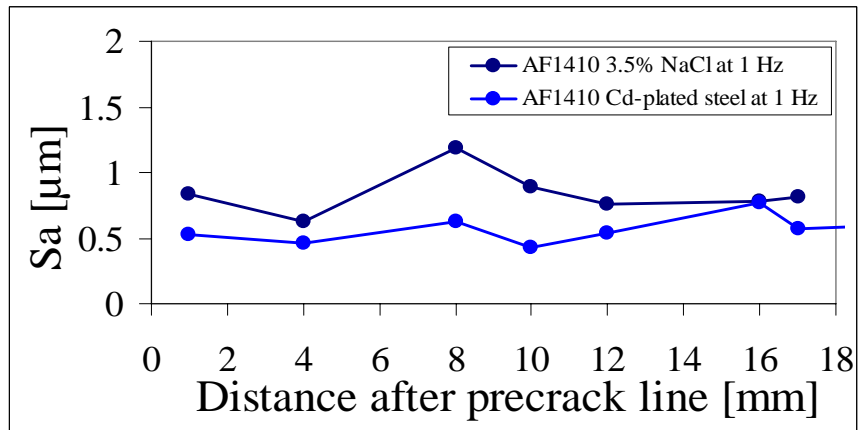


Figure 2.14 Roughness average vs. distance from precrack line in AF1410 steel. a) 1% NaCl at 1 and 0.5 Hz; b) 3.5% NaCl at 1 and 0.5 Hz; c) 1% NaCl and 3.5% NaCl at 1 Hz; d) 1% NaCl and 3.5% NaCl at 0.5 Hz; e) Cadmium plated steel and 1% NaCl at 1 Hz; f) Cadmium plated steel and 3.5% NaCl at 1 Hz

The AF1410 steel and aluminum alloy AA7075-T6 fatigue life calculations were estimated by the crack growth rate da/dN . This expression is presented in terms of the stress intensity factor range ΔK ($K_{\max}-K_{\min}$), the constant A ($\text{MPa}^{-n} \cdot \text{m}^{1-n/2}/\text{cycles}$) and the exponent n . This equation is identified like the Paris law for stage II (Equation 2.4) [27].

$$\frac{da}{dN} = A(\Delta K)^n \quad \text{Equation 2.4}$$

Results showed that at low frequency (0.5 Hz) the corrosion fatigue crack growth (CFCG), represented by da/dN . The crack growth rate increased significantly in both 1% and 3.5% NaCl solutions as revealed in Figure 2.15. The pH in the crack tip was acidic, approximately 2.5 while the bulk solution was practically neutral [28]. The Cl^-/H^+ oxidant potential is major at pH low. Therefore, the passivation film rupture and is followed by the dissolution of the exposed metal surface (particularly notable under stress). In this reaction, the oxidant agent was the acid while the chloride ions aided at the corrosion sub-products formation (oxides). This explains the severe corrosion process promoted in the AF1410 steel.

Reduction in lifetime at 0.5 Hz frequency was greater in 3.5% NaCl solution compared to 1% NaCl. This physically meant that the crack propagation implicated ionic diffusion of chlorides ions with catastrophic effects on the material. Therefore, on the steel surface occurred the rupture of passivation film, followed by the exposed metal surface dissolution (particularly under stress) attributable to local metal loss. In consequence, an elevated percentage of NaCl enhanced the concentration of aggressive chloride ions with catastrophic effects on the material.

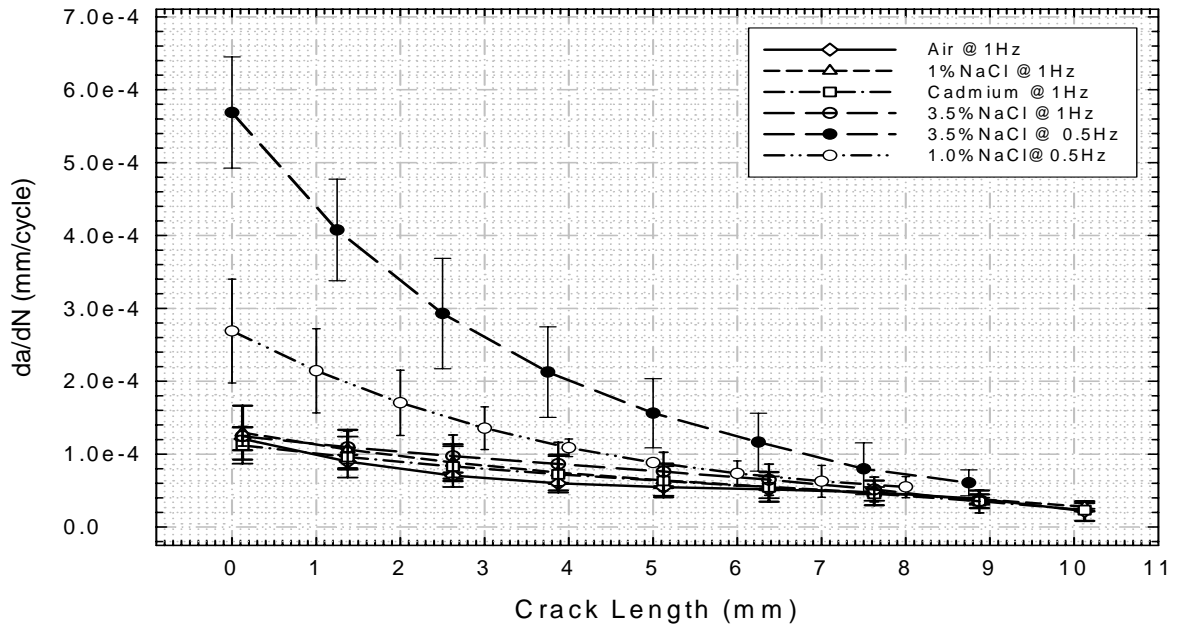


Figure 2.15 Average results of CFCG shown for AF1410 specimens

2.5.5 Roughness changes and crack growth propagation

Modification in the mechanical properties, as a consequence of electrochemical and micromechanical processes in the crack tip during the simulated marine environment exposition. The da/dN obtained on AF1410 sample exposed at 3.5%NaCl solution with a frequency of 0.5 Hz, increased as Figure 2.15 reveals. Therefore, it was expected that the fracture surface at a high saline concentration had a higher roughness average. However, when the %NaCl was reduced and at low frequency (Figure 2.14 (a)) the plot exhibited a higher average roughness than the sample exposed to higher %NaCl (Figure 2.14 (b)).

In addition, cadmium plating on the surface of AF1410 steel was carried out to improve the adsorption and dissolution of atomic hydrogen. However, it appears that permeation into the sample was achieved only for small depths (possibly $<10^{-3}$ cm [28]). As a result, the specimens tested under saline solution exhibited higher roughness parameters than the fracture surface for the cadmium plated steel sample effect caused by the corrosion process on the fracture surface. Whereas, cadmium plating specimen did

not experiment embrittlement process on surface fracture due to hydrogen permeation as was expected. As a result of this, it did have a flatter fracture than specimens exposed at %NaCl.

In summary, the roughness parameters in the analyzed fracture surfaces, such as: average, mean and root mean square values on AF1410 steel kept the proportion between them. With respect to the S_p and S_y parameters no clear tendency was observed for different testing conditions (frequency and solution concentration). All the plots exhibited too large variability in S_p values due to large height differences in peak values. Since the S_y parameter is the difference between S_p and S_v , the variability of S_p affected heavily the S_y values.

Other authors [29] used the lowest measured height S_v to compare surfaces with deposits of corrosion in metallic materials. In this work, the specimen tested in air had a $S_v = -2.85 \mu\text{m}$ while the sample exposed to 1% NaCl showed a $S_v = -5.02 \mu\text{m}$. Clearly the S_v parameter serves as an indicator of corrosion deposits on the sample.

The analysis of fatigue results (Figure 2.15) required considering a number of factors. Thence, it was possible to estimate the frequency and %NaCl effect on the crack growth rate. Nevertheless, the effect of saline concentration and frequency can not be determined by roughness parameters alone since the AF1410 fracture surface was too irregular along the crack propagation path. In addition, it was corroborated that AFM is a technique to study a specific study area over the whole fracture surface.

Furthermore, a fractal study of the AF1410 steel fracture can provide a possible relationship between the fracture surfaces and da/dN , using the same images obtained by the AFM.

2.6 Fractals in fractured surfaces

The use of fractal analysis have been widely increasing given by the study of irregular forms in the nature; including fracture surfaces. The fractal analysis purpose consisted in confirm the self-affinity properties of the AF1410 fracture surfaces.

Besides of roughness parameters studied before, additional conclusions about this steel were necessities to demonstrate the saline environment and frequency effects in the high performance AF1410 steel. In this study, rough forms revealed in the AF1410 steel fracture surfaces were analyzed using fractal analysis.

Fractal objects show a fractal dimension and exactly the same characteristics or forms independent of the degree of magnification or scale used. This property is known as self-affinity. Self-affinity surfaces are observed as perpendicular fluctuations with respect to a reference plane. Such height fluctuations through a determined longitudinal scale (r), in which its direction is parallel to the reference plane, present scaled properties characterized by the roughness exponent (ζ) [30]. This exponent magnitude range goes from 0 to 1. When the surface is completely flat the value of the roughness exponent is equal to one. If ζ decreases the roughness increases; so the roughness is inversely proportional to these exponents value. The self-affinity behavior in real surfaces is presented up to a determined longitude in a scale called correlation longitude (ξ). Above this value surfaces are determined to be planes and its dimension value is equal to two. Fracture surfaces are self-affinity objects. In ceramics and metals their surfaces exhibit a roughness exponent equal to 0.8 along 10 to 30 units of longitude. This enables the establishment of the universal conjecture for this exponent independent of the type of material and fracture mode. This self-affinity regime is found under elevated fracture propagation conditions and lengths in the micrometer order.

Features of fractured surfaces are determined by material properties, the initial defect size and the stress states. Then, fractography establishes the relationship between

the bond-breaking process and the fracture surface topography. Fractal geometry (or the geometry of the degree of the roughness) quantifies this relationship.

In fractals, the scaling exponents are not affected by microscopic variations of the system under study; on the contrary, they only reflect internal symmetries. The growth processes are classified according to the characteristic values of these exponents, related to intrinsic dynamical processes of the system [31].

2.6.1 Fractal background

Aldaco *et al.* [32] presented the self-affine analysis of the fracture surface of an A319 casting alloy. Fracture surfaces were analyzed using a scanning electron microscope, contact atomic force microscopy and a stylus profilometer. The first quantitative self-affinity analysis was performed for length scales spanning over seven decades in logarithmic scale, from the nanometer to the centimeter scales. The variable bandwidth method was applied to calculate the roughness exponent and the correlation length for this alloy. For the roughness exponent, a value of $\zeta \approx 0.8$ was obtained, which was close to that reported for other materials broken under similar kinetic conditions. The correlation length was found to be related to the largest characteristic lengths of the microstructure.

In 1984, Mandelbrot *et al.* [33] suggested that the fracture surfaces are natural anisotropic nature fractals per se; their self-affine character is accepted almost universally. Bouchaud [34] proposed the idea of a universal roughness exponent, $\zeta = 0.78$ independent of the microstructure and the material properties. This universality was seriously questioned for the discovery of other self-affine regime characterized by a roughness exponent $\zeta = 0.5$ to fractured surfaces in slow crack propagation conditions and analyzed in nanometric scales by means of atomic force or scanning tunneling microscopy. Recently, the coexistence of both regimens has been revealed in different materials. Hinojosa [34] supports the idea that crack front, considered as one line, interacts with the different obstacles present in the microstructure and through this the major heterogeneities are those that must determine the correlation length.

The power law growth used to find the AF1410 Hurst exponent was introduced by A. L. Barabási *et al.* [14] through scaling concepts presenting a ballistic deposition (BD) model. By definition, when a particle is released from a randomly chosen position above the surface located at a distance larger than the maximum height of the interface; the particle follows a straight vertical trajectory until it reaches the surface, whereupon it sticks. The deposited particles form a cluster with a very particular geometry. The interface growth starts from a horizontal line; that is to say, at time zero the interface is simply a straight line, with zero width. As deposition occurs, the interface gradually roughens. A typical plot of the time evolution, ' t ', of the surface width ' w ' has two regions separated by a crossover time ' t_x ' (Figure 2.16). Initially, the width increases as a power-law, but this behavior does not continue indefinitely, due to the fact that an asymptotic regime reaches saturation value, the horizontal region in Figure 2.16 can be identified two characteristic regimes: (1) power law growth, which appears as a straight line on the log-log plot, and (2) saturation [14].

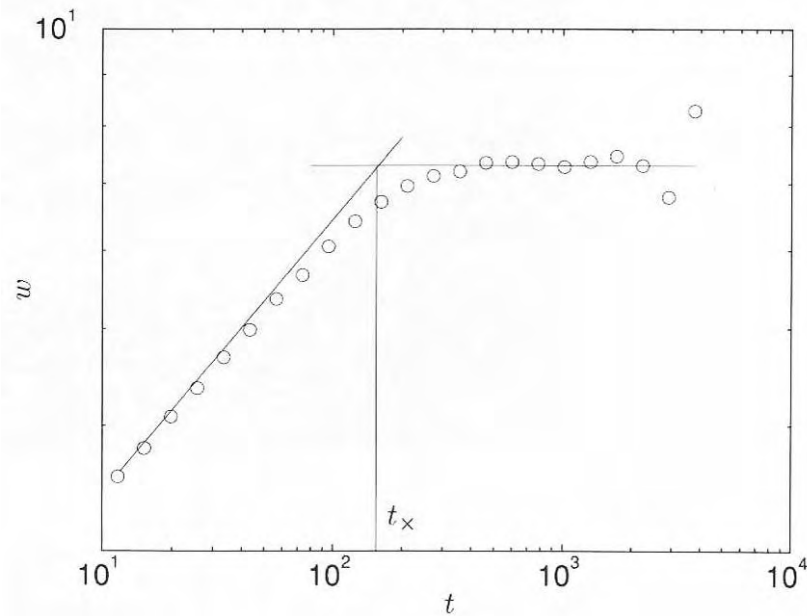


Figure 2.16 Growth of the interface with time for the BD model [14]

In this research, the self-affinity of the AF1410 steel was investigated with the same AFM images analyzed in section 2.5, in order to correlate the Hurst exponent with fatigued sample conditions, such as frequency and saline concentration of the electrolyte used to simulate marine environment.

To determine the Hurst exponent ζ for fractured AF1410 specimens by using height profiles, the band width method was used. This method is detailed in the following section.

2.6.1.1 Variable bandwidth method

Once the AFM captures an image of the AF1410 steel, it generates a data matrix in ASCII code of 512x512 data points. Each value of this matrix corresponds at one height (z_k) in the x_i, y_j coordinates. Figure 2.17 displays the profiles of an AF1410 sample tested at 25 °C and atmospheric pressure. These two parallel profiles were obtained using a fast scanning rate at 1 mm distance from the pre-crack and perpendicular to the crack propagation direction. Using the variable bandwidth method, 512 of these profiles were divided into windows of width r each one. Therefore, there are 511 profiles and when $r=1$ (window width=2 values, a maximum and a minimum); for the first profile we have 511 values according to Equation 2.5. The difference in absolute value between the maximum and minimum heights in the profiles is presented by Equation 2.6. In this equation, the ZH value represents the difference between the value in Z higher and the lowest, in a window, and it was computed for each window, and then averaged over all the possible windows (moving average method).

$$\frac{\#Pixels}{window\ width, r} \Rightarrow \text{If } r = 1: \frac{512}{r} - 1 = 511; \quad r = 2: \frac{512}{2} - 1 = 255 \quad \text{Equation 2.5}$$

$$ZH(i, j) = |ZH(i, j \cdot r + 1) - ZH(i, j \cdot r + 1 - r)| \quad \text{Equation 2.6}$$

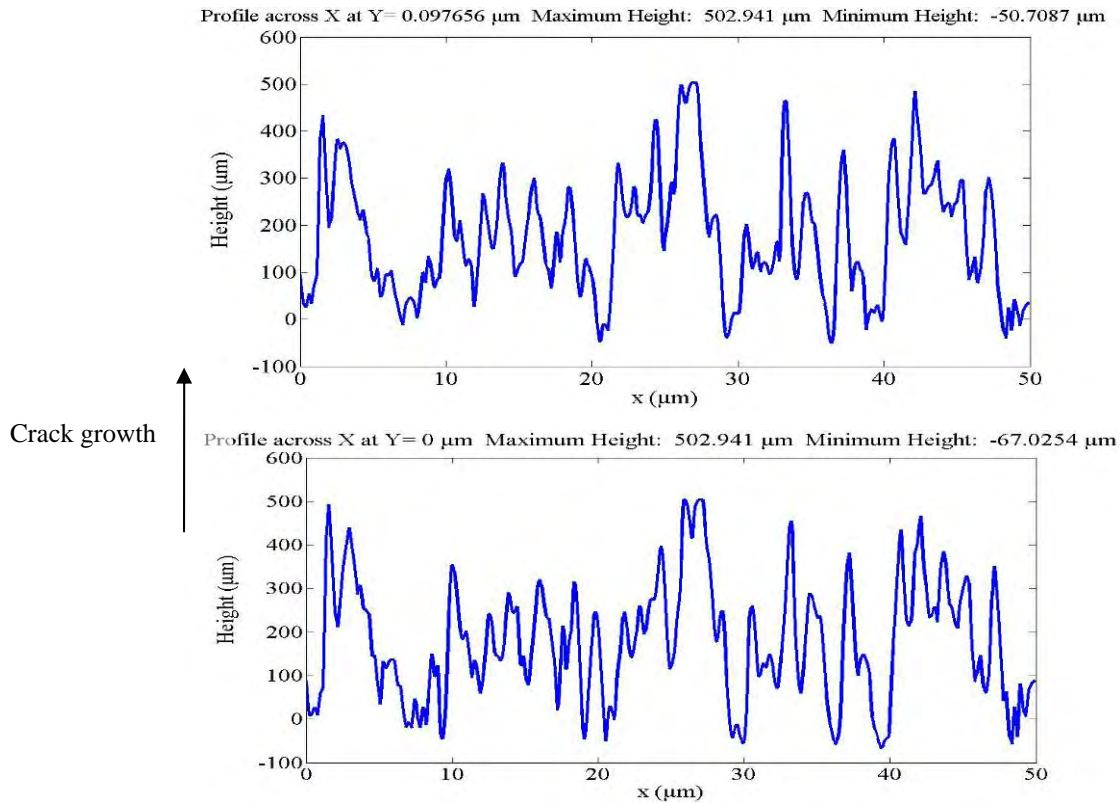


Figure 2.17 Longitudinal profile corresponding to the crack growth sense

2.6.2 Hurst exponent

AF1410 steel samples were used to estimate the Hurst exponent, trying to find if there was a relationship between the distance of the precrack line and the roughness of the surface. Over each sample eight different areas were measured at different distances from the precrack line (1, 4, 8, 10, 11, 12, 16 and 17 mm).

The size of the scanned area was $2519.6 \mu\text{m}^2$ corresponding to a nominal $50 \times 50 \mu\text{m}^2$ area, for the estimation of the roughness exponent. This was the area considered in the Hurst exponent calculations. For each image 512 height profiles perpendicular to the fast scan direction were taken. The calculation of the roughness exponent in each sample was carried out using the variable bandwidth method. To determine Hurst exponent ‘ ζ ’ or roughness exponent, a Matlab[®] code was written (see Appendix). SPIP[™] allows saving

the image in 3D in ASCII format. This information was utilized to collect the profiles corresponding to the AFM images.

2.6.3 Results and Analysis

Z_{prom} , in Figure 2.18 is the axis of ordinates, where every value corresponding at a '*Z average*' over 512 profiles. This value was obtained to each width of window '*r*' (1, 2, 3, etc.). Consequently, Z_{prom} (μm) vs. *r* on a logarithmic – logarithmic scale produces a straight line (for lower '*r*' values) with the slope equal to the roughness exponent ζ .

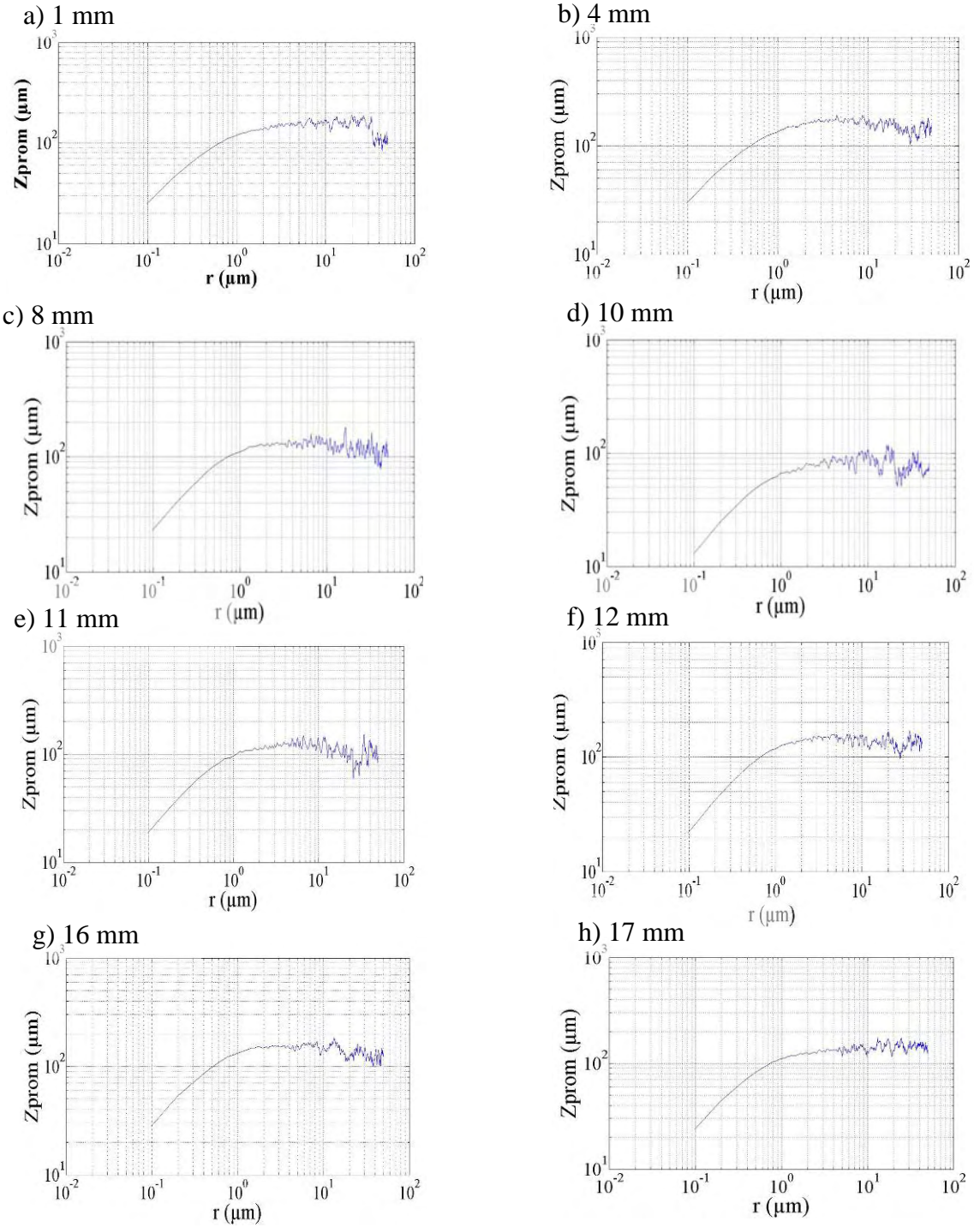


Figure 2.18 Hurst exponent in AF1410 at air conditions at 3 Hz in an area of $2519.6 \mu\text{m}^2$

The self-affine behavior of fracture surfaces of AF1410 steel tested under six different conditions was analyzed applying the variable bandwidth method to the height profiles generated with the AFM (Figure 2.18). The roughness exponent ζ obtained was ≈ 0.5 with a standard deviation of 0.028. These results are in excellent agreement with the recognized $\zeta=0.5$ cited in the literature for metallic materials. Figure 2.19 shows self-affinity results analyzed for six AF1410 samples. The results indicate that AFM data is perfectly consistent with the value reported by Hinojosa *et al.* [35] and Parisi *et al.* [36].

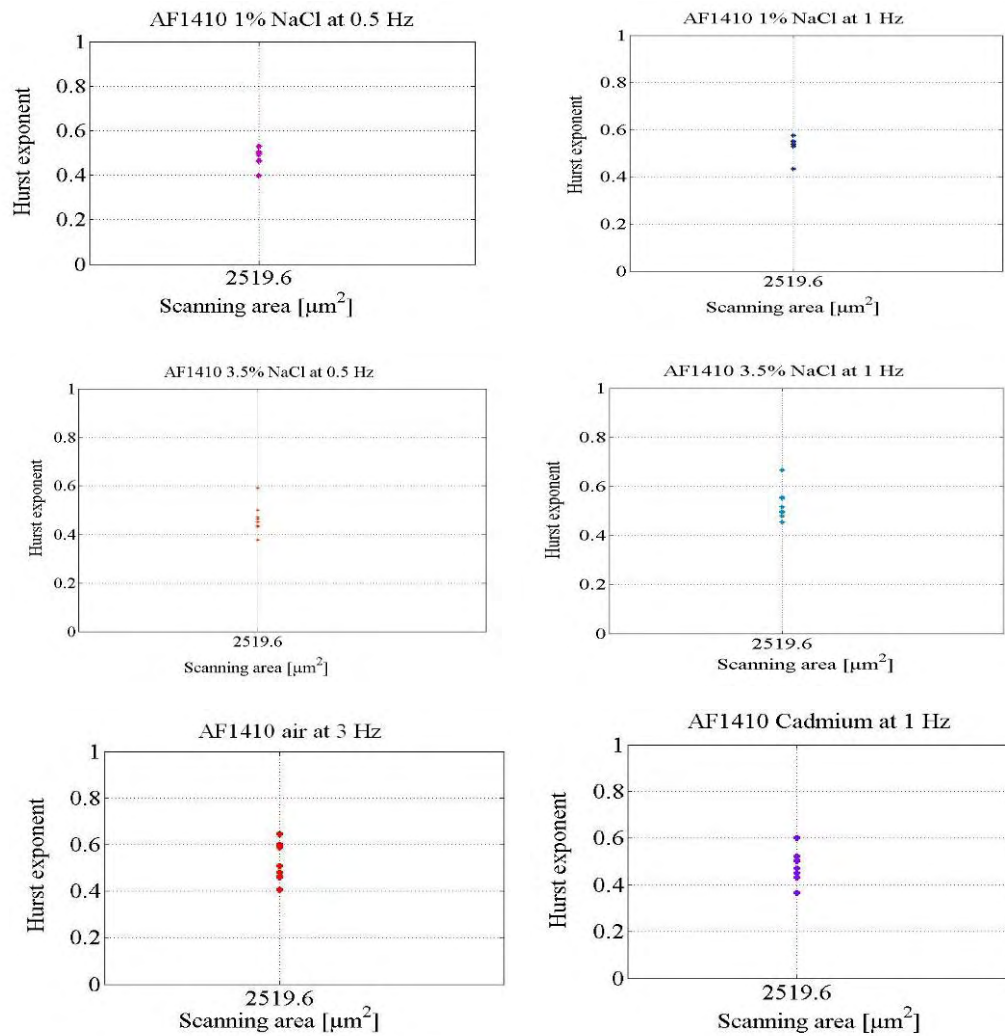


Figure 2.19 Hurst exponent in AF1410 using a 50 μm scan range

Table 2.4 presents the Hurst exponent mean values corresponding to the eight points analyzed in each sample at 6 different conditions. The table data was obtained directly from the plots shown in Figure 2.19 for the respective conditions.

Table 2.4 Mean Hurst exponent in AF1410 samples

Material conditions	$\bar{\xi}$
In 1% NaCl at 0.5 Hz	0.4787
In 1% NaCl at 1 Hz	0.5313
In 3.5% NaCl at 0.5 Hz	0.4651
In 3.5% NaCl at 1 Hz	0.5265
In air at 3 Hz	0.5185
Cadmium electroplated at 1 Hz	0.4852

To compare the effects of sodium chloride concentration and loading frequency on the steel fracture, four graphs were prepared using the roughness average (S_a) and Hurst exponent values (Figure 2.20).

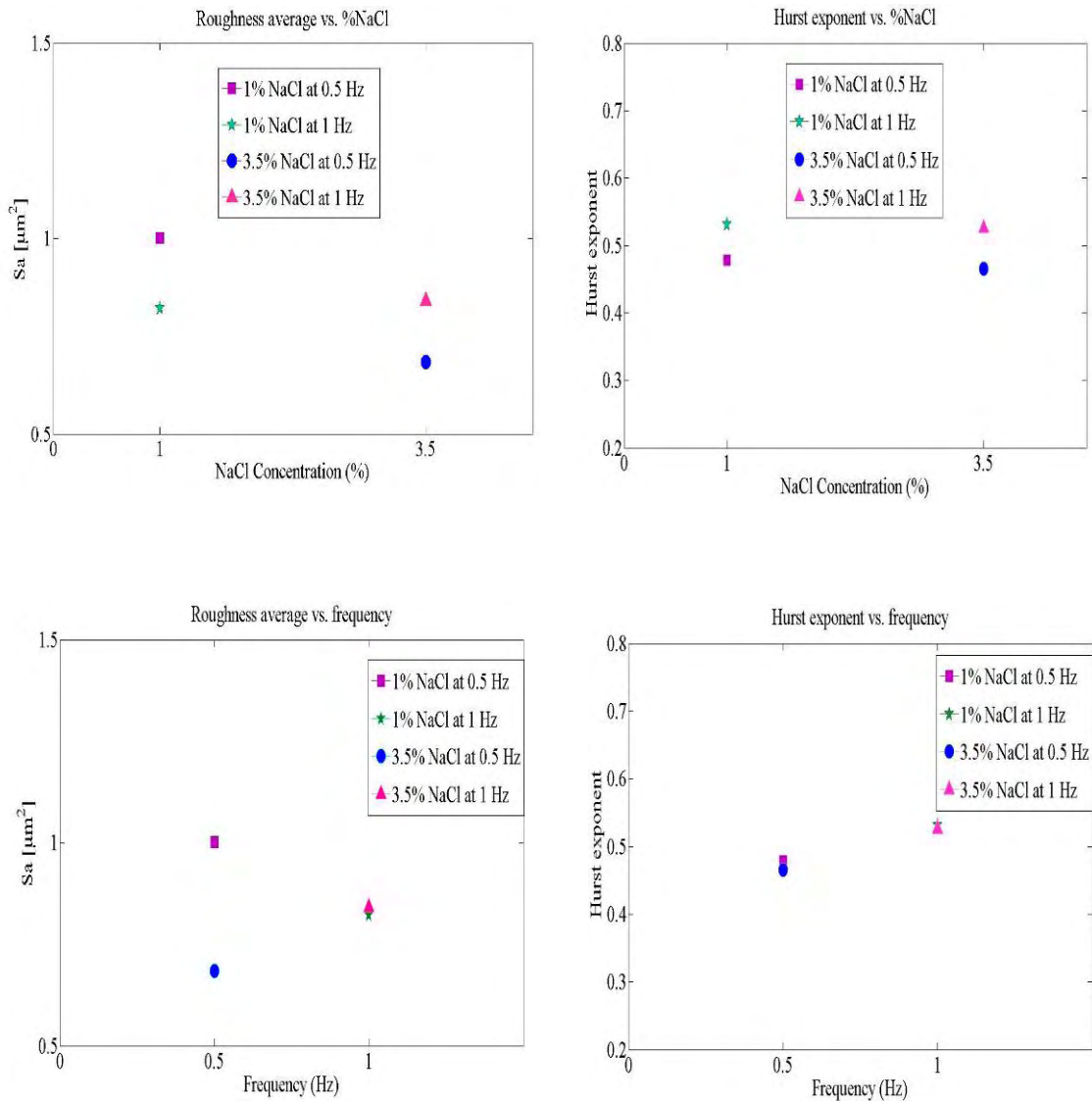


Figure 2.20 Roughness and Hurst exponent dependence at frequency and NaCl concentration

For each plot in the Figure 2.18, the Hurst exponent was computed at one distance from the precrack line (1, 4, 8, 10, 11, 12, 16 and 17 mm). These distances were determined on the specimen using a ruler and a market. These exponents were represented as data points in Figure 2.19 and their mean values displayed in Table 2.4. These values were found in order to correlate fractured surface features with crack propagation characteristics. In the microfracturing experiment for small length scales (50 μm), a value of $\zeta \approx 0.5$ was found for the roughness exponent (Table 2.4). More extended studies have also observed the same roughness exponent value ($\zeta \approx 0.5$) in experimental

conditions for fractured surfaces in metallic materials [36]. The two values of the roughness exponent are associated of this form: $\zeta = 0.5$ for small length scales and $\zeta = 0.8$ for large scales. The crack front growth is connected with $\zeta = 0.5$ and is interpreted as a quasi-static regime. According with that, all the samples were tested as quasi-static regime, at 8.4N/s yielded average ultimate static strength of 39-kN for AF1410 [28]. This connection comes from the suggestion that the crack surface can be thought as the trace left by the crack front.

In the two left plots showed in Figure 2.20 (roughness average vs. % NaCl and roughness average vs. frequency), the sample fatigued at low frequency and low saline concentration, revealed the maximum roughness average due to the precipitates produced by the corrosion process. An increment in the frequency during the fatigue test induced higher Hurst exponents in samples exposed at sodium chloride (Figure 2.20).

Studying the AF1410 fracture surface through fractal analysis, the relation between the Hurst exponent and any important feature of the fatigue experiments was not found due to the lack of saturation level.

In order to verify the fractal contribution at the fracture process, it will be convenient to perform a model into the fractal analysis, relating AF1410 fracture toughness (K_{IC}) with fractal dimension (D) evaluated at diverse simulated environment conditions.

3 HYDROGEN EMBRITTLEMENT EFFECT ON AF1410 STEEL

The performance of arresting shanks and landing gears made of AF 1410 steel used in critical service conditions (large impact loads, engine exhaust gases, excessive high flight loads and marine atmosphere with chlorides anions) was evaluated under fatigue by charging the samples with hydrogen.

Morphological analyses of fracture surface can offer reliable information about AF1410 steel behavior under hydrogen entrance. This process takes place while melting, electroplating and during service when subject to wet environments occurring at the same time as the corrosion process. This is of particular interest since AF 1410 steel due to its high toughness, high ultimate tensile strength and appropriate corrosion resistance is widely used in severe marine conditions. However, the steel chemical composition and the martensitic structure make it susceptible to be attacked by hydrogen and undergo an embrittlement process. Therefore, fatigue tests and morphological surface analysis were performed in order to understand the effects of hydrogen permeation into the material as a damaging agent, reducing lifetime and mechanical resistance.

The main task of this chapter is to understand the fatigue behavior and to analyze the fracture surface features to obtain a better understanding about the changes in fracture modes due to combined action of environmental and mechanical conditions of hydrogen embrittled AF1410 steel. Therefore, the fracture behavior of AF1410 specimens, charged cathodically with hydrogen was characterized through different techniques, AFM and SEM.

3.1 Experimental setup

The sample preparation was carried out as described in 2.3.1. Then the specimens were charged with hydrogen using a Solartron 1280. The cell used for the permeation of hydrogen into the steel is shown in Figure 3.1.

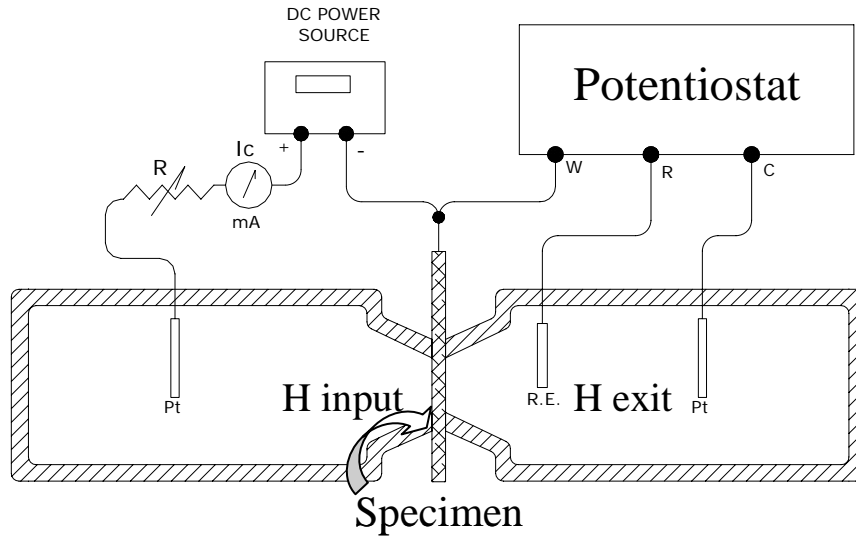


Figure 3.1 Electrochemical cell for hydrogen permeation

The mechanism involved with hydrogen permeation into the steel was originated with the hydrogen transporting through a solution phase, then adsorbed, absorbed and finally diffusion. This hydrogen transport was enhanced by dislocation presence in the AF1410 steel [37].

The hydrogen damage was the result of lattice decohesion mechanism by which, the atomic bond energy was low in the presence of hydrogen.

The specimen was charged cathodically with hydrogen (input) for 236 hours on one side and with a current density $=0.31 \text{ mA/cm}^2$, anode area $= 1.89 \text{ cm}^2$ immersed in 0.1M NaOH solution. The cathodic area was 6.43 cm^2 and the electrode was immersed in 0.1M $\text{H}_2\text{SO}_4 + 1 \text{ g/l Na}_2\text{HAsO}_4 \cdot 7\text{H}_2\text{O}$ solutions. An arsenic concentration between 0.25 – 1.00 $\text{Na}_2\text{HAsO}_4 \cdot 7\text{H}_2\text{O}$ into the AF1410 steel accelerates hydrogen entrance [37]. Specimens were fatigued after charging and for control fatigue testing a MTS 810 tensile testing machine with COD gauge was utilized (Figure 2.6). Conventional crack growth tests were carried out on pre-cracked specimens under a maximum stress, $\sigma_{\text{max}} = 1,620 \text{ MPa}$, a stress ratio of $R = 0.4$, $K_I = 21518 \text{ lb}\sqrt{\text{in}}$, frequency of 1 Hz (with sinusoidal loading) and 95000 cycles. AFM (EasyScan[®] Atomic Force Microscope) and scanning electron microscopy techniques were used to determine differences between hydrogen

charging input side and output one. All secondary electron images were obtained in the JEOL JSM 6100 electron microscope of Materials Science Center at the University of Wisconsin-Madison.

3.2 Analysis of results

In order to observe the effect of the hydrogen in the fatigue crack growth and compare it with the output side at the end of the crack tip Figure 3.2 is shown. These images were taken before final fracture and after hydrogen charging.

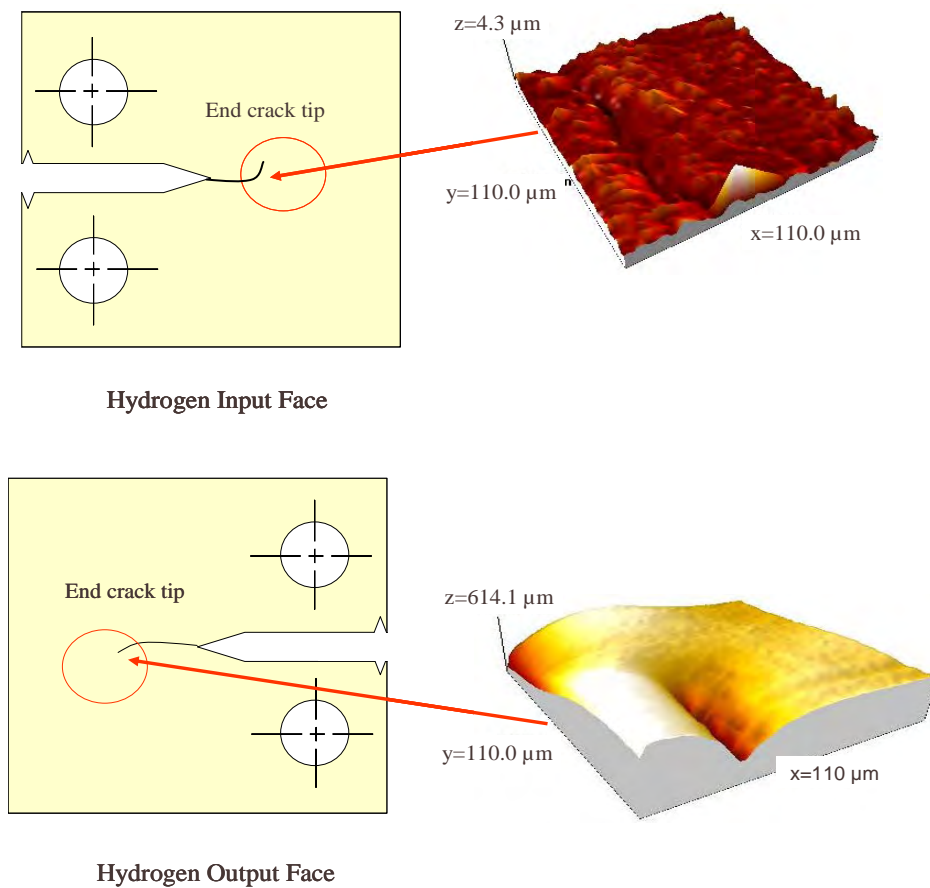


Figure 3.2 Specimen input hydrogen face (roughness average $0.223 \mu\text{m}$), output hydrogen face (roughness average $0.0879 \mu\text{m}$)

The high roughness value, $0.223\ \mu\text{m}$ in Figure 3.2 is product of a more aggressive environment

According to Figure 3.2 the roughness average (S_a) in AF1410 steel is larger in hydrogen input face than hydrogen output one. This roughness difference can be observed in the Figure 3.3. In this micrograph, the upper image corresponds to the H-charged side while the bottom one is the non-H affected region.

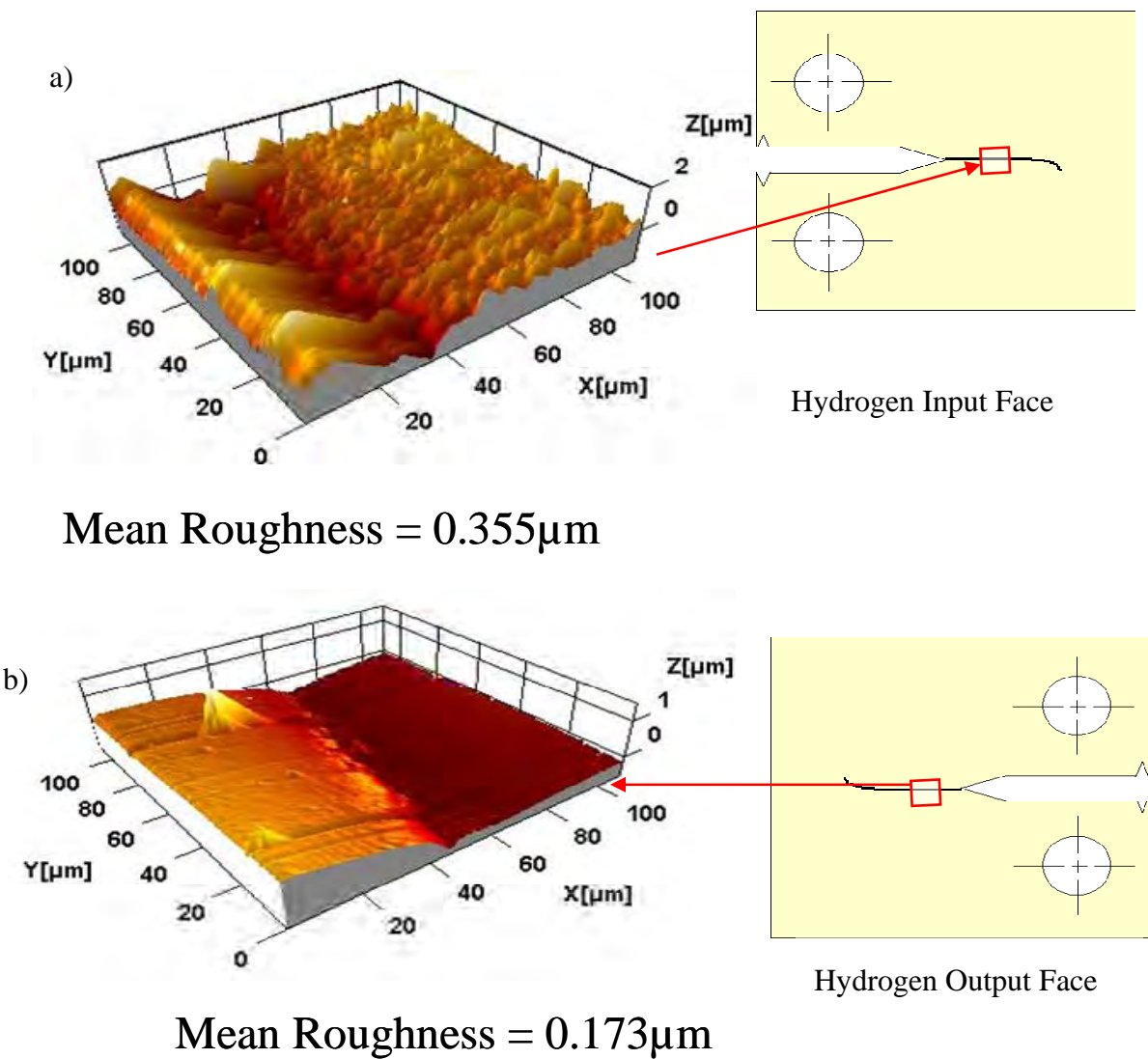


Figure 3.3 AFM images over crack way in the AF 1410 steel. a) H-charged side; b) non-affected region

The qualitative and quantitative information obtained in Figure 3.3, were the visual appearance of the crack tip in the specimen and hydrogen effect in the roughness surface. The upper image exhibits a superficial damage (uniform pitting corrosion due to the presence of H^+) of the specimen where the hydrogen permeation was performed. Clearly the effect of environmental damage due to hydrogen is observed; this is also reflected in the high roughness measured by the AFM. The bottom image corresponds to the surface at the output side where the surface remains unaltered. The smoothness of the surface (smaller roughness) is apparent as well as the local lateral plastic deformation.

The results of crack propagation rate in tension fatigue testing were measured during fracture on compact tension specimens under air and hydrogen charging. A gage extensometer was attached across the opening of the crack, as sketched in Figure 2.6. Thus, the crack tip velocity (da/dN) was monitored continuously during fatigue. The crack growth rate vs. crack length curve for the AF 1410 steel under hydrogen permeation is shown in Figure 3.4. Here the two curves display da/dN decreases, versus crack length increases. In the sample with hydrogen at 1 Hz of frequency, the da/dN diminished drastically with increasing crack length.

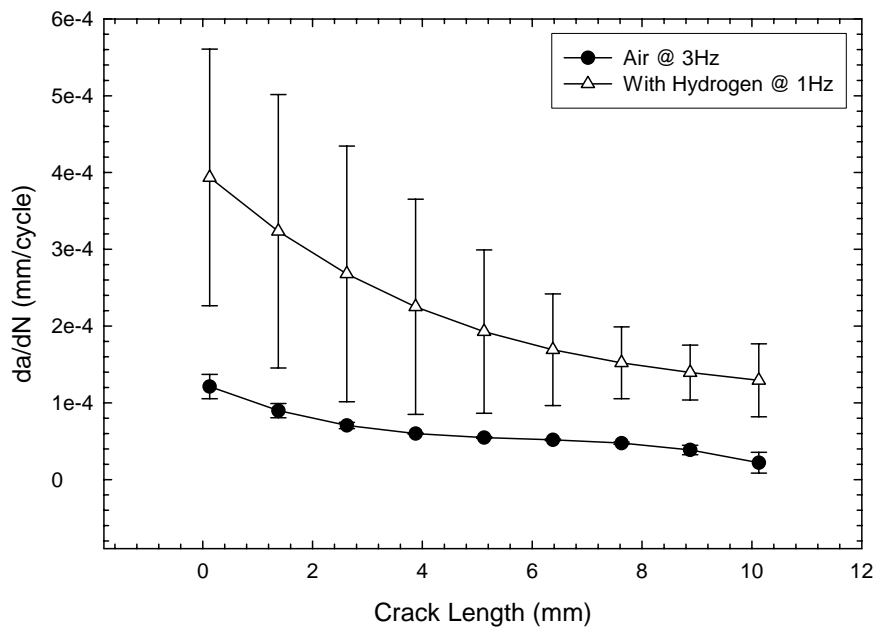


Figure 3.4 Crack growth rates as a function of crack path

Although the frequency in air and hydrogen conditions in the Figure 3.4 was different, the data were used to appreciate the significant crack growth increases in the hydrogen charged specimen. The hydrogen effect in the AF1410 steel generated a short lifetime in the material as shown in Figure 3.4 which contains the crack length vs. da/dN .

AFM images were generated with a z-range (height) of $20\ \mu\text{m}$ in a square area of $12,100\ \mu\text{m}^2$ at distances of $0.5\ \text{mm}$ from the line of the precrack. Figure IV.7 displays the AF1410 fatigued specimen tested under hydrogen charge. The SEM photograph was taken at $0.5\ \text{mm}$ distance from the pre-crack. The measured roughness values corresponding to these images were: $1.75\ \mu\text{m}$ in the hydrogen-charged side and $0.71\ \mu\text{m}$ on the output side. In the SEM micrograph, the upper right side corresponds to be clearly correlated with the hydrogen charged region while the bottom left side is the non-hydrogen affected region.

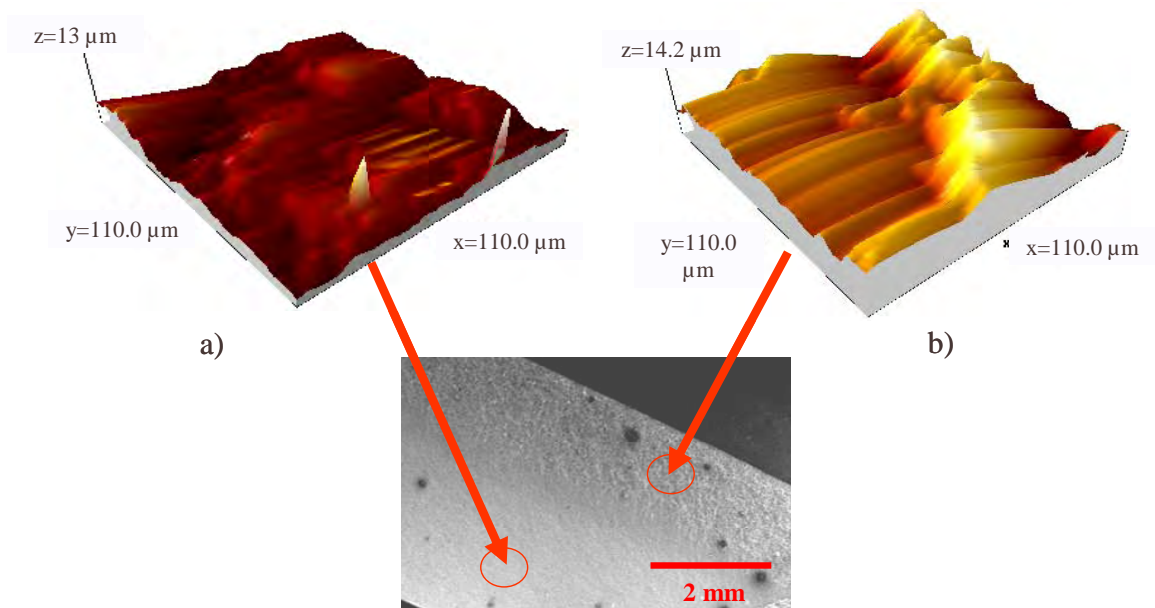


Figure 3.5 Scanning electron microscope Image of a hydrogen charged specimen of AF1410. a) Hydrogen non-affected zone (roughness average $0.71\ \mu\text{m}$), b) Hydrogen affected zone (roughness average $1.75\ \mu\text{m}$)

The fractured surface was analyzed through SEM. The images obtained at a distance of 4 mm from the precrack ($a=4$) in crack growth direction are shown in Figure 3.6.

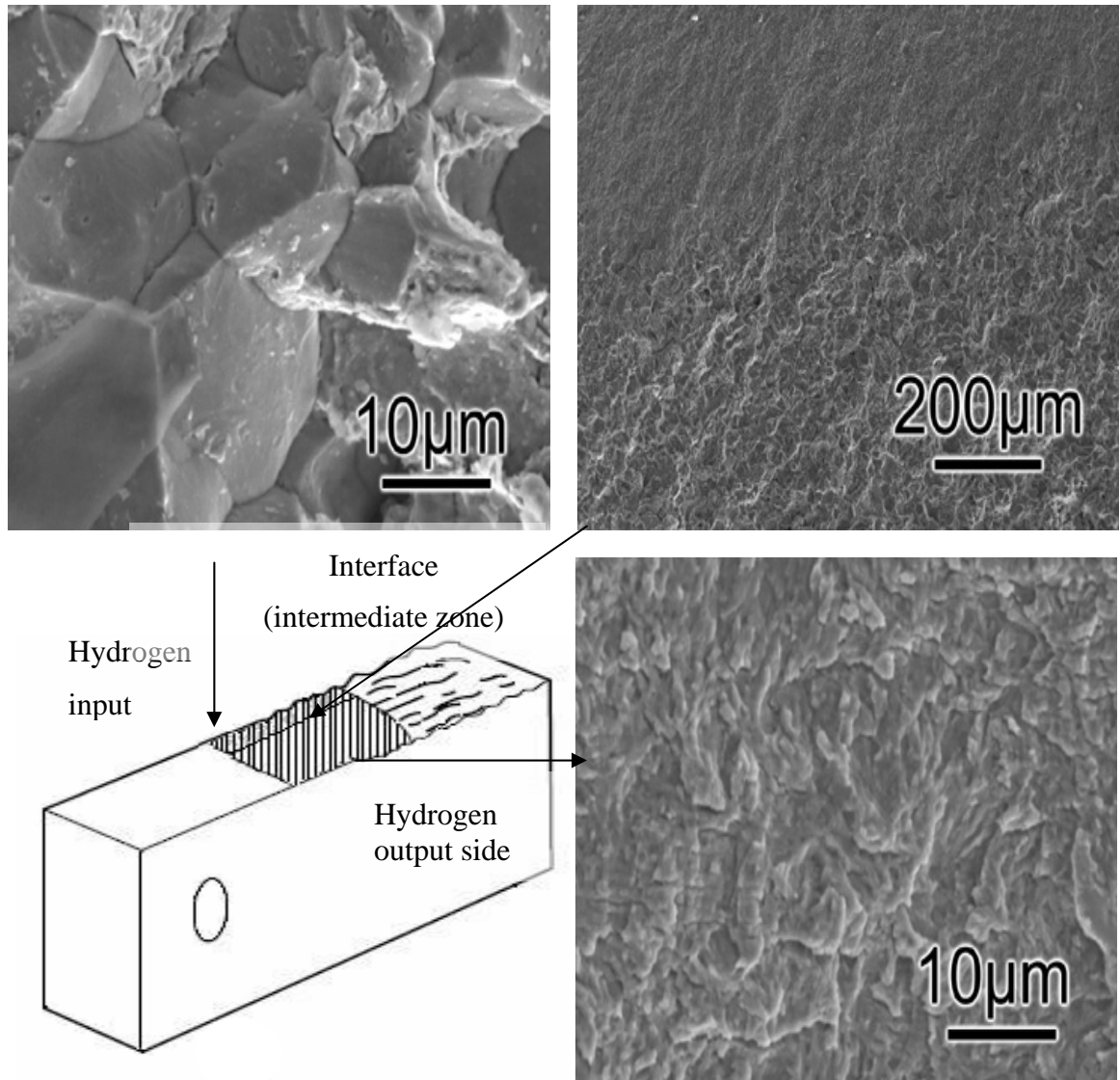


Figure 3.6 Fracture surface specimen (fast crack growth velocity)

These SEM images show fracture mode changing due to hydrogen embrittlement. The interface region displays the extent of the embrittlement (lower portion) with mostly

intergranular fracture. The fracture mode changes from ductile behavior to brittle manner as shown in these images. The local crack growth rate was $da/dN=1.2449 \cdot 10^{-4}$ mm/cycle, that corresponds at fast crack growth rate. Figure 3.7 for a slower crack growth rate than Figure 3.6 reveals the same differences observed between these images, where fracture mode was principally affected by the presence of hydrogen.

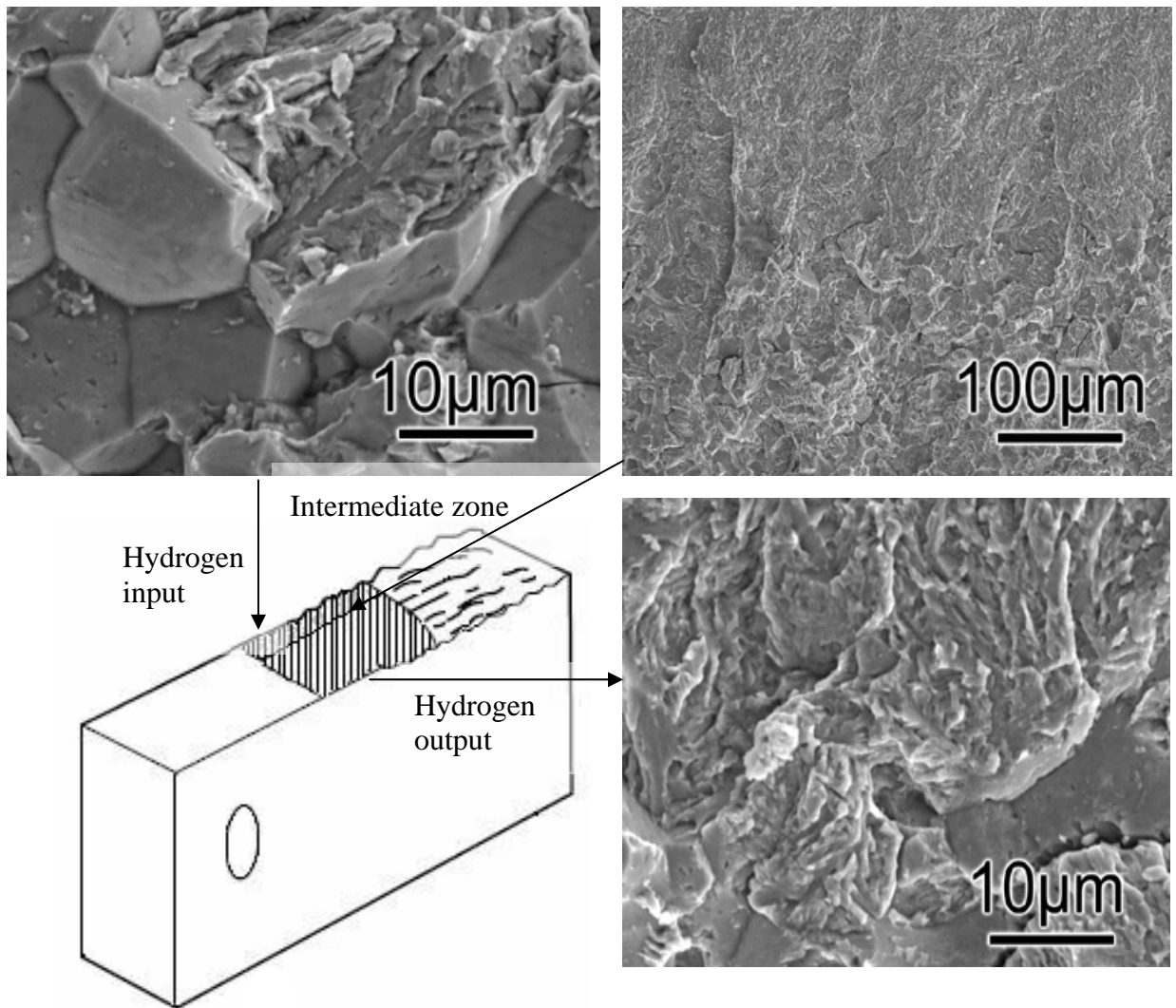


Figure 3.7 Fracture surface specimen (slow crack growth velocity)

Figure 3.7 represents a zone at 4 mm of distance from the crack tip, where local crack growth rate was $da/dN=3.3 \cdot 10^{-4}$ mm/cycle, slower than Figure 3.6. A common feature in Figure 3.6 and Figure 3.7 (more evident in the last one) was that fracture in hydrogen input a combination of intergranular fracture and patches of dimple ductile was present. This intergranular fracture zone on the hydrogen input face was prevalent in both specimens. Furthermore, the SEM micrograph of fracture surface in Figure 3.7 of this region was surrounded by the dimple ductile fracture. In summary, the fractographs of the AF1410 steel present intergranular fracture due to hydrogen embrittlement and ductile fracture in the intermediate zone between hydrogen input and hydrogen output. Hydrogen reduced the ductility in the area submitted under charging condition. The SEM fractographs of the failure surfaces showed evidence of intergranular cracking. This cracking decreased with the depth of charging and evidence of microscopic ductility was found in the non-charged zone in the specimens.

The effects of hydrogen on the mechanical properties of AF1410 steel included a faster crack growth rate and reduction in ductility. The fatigued specimens displayed intergranular fracture with a depth that was proportional inversely to the ten days of hydrogen charging time.

Fracture modes were affected by hydrogen permeation into the AF1410. According to the literature, the higher the strength of the steel, the lower the critical hydrogen level necessary to induce embrittlement. In the sample tested under hydrogen, intergranular and transgranular fracture modes were observed, which drives to a brittle fracture. While a specimen tested in air demonstrated a ductile fracture with microvoids coalescence in the material, then, a ductile to brittle transition was observed in the material particularly in the intermediate zone. As a consequence, the environmental embrittlement process has significant influence in fracture modes transitions.

4 GRAIN ORIENTATION IN ALUMINUM ALLOY 7075-T6 FRACTURED IN FATIGUE TESTING

Aluminum and high strength steel alloys are materials used in the aeronautical industry. For such reason the fractographic study of these materials is of great interest in engineering. The grain orientation effect in the AA 7075-T6 alloy was evaluated in order to correlate the different crack growth rates developed by the same alloy in impact-fatigue test.

In addition, the 7075 alloy is the strongest and stiffest of the commonly available aluminum alloys. The high performance is developed by its T6 condition becoming in the most machinable alloy in rod and bar form [38]. T6 means: solution heat-treated at 250° F (artificially aged) and allowed to cool at room temperature [39].

In this chapter we will study the morphology of the fatigue crack in rolled 7075-T6 aluminum flat stock fatigued in two directions. One with the notch oriented parallel to the rolled direction (transversal) and the other perpendicular (longitudinal).

4.1 Influence of grain orientation in the fracture behavior of Al-alloy

A previous work on 2023-T3 alloy found a strong function of the Mode I crack tip opening displacement (CTOD) on the orientation of the crack relative to the rolling direction; CTOD for a transversal specimen was 0.84 mm, increasing linearly with orientation angle to 1.05 mm for a longitudinal case [35].

In other studies [40], a sequence of Fourier transform techniques were used to investigate the effect of microstructure on the fatigue mechanism in AA 7075-T6. In this work, standard charpy-size specimens were used to study crack growth using Fourier

spectrum analysis. The length of the specimen was parallel to the rolling direction and the fatigue crack was designed to propagate across the transverse direction. The progress of the fracture in the transverse direction interacted with grain boundaries and microconstituents that were contained within the plastic zone of the crack tip [40].

The effects of grain orientation on the fracture behavior of aluminum alloys have received some attention. Crack tunneling behavior for Mode I loading of T-L and L-T cases was studied by other authors [41]. Their work showed that crack growth was largest in the T-L specimen, occurring throughout the crack growth process. The effect of grain orientation on CTOD for mode I loading was studied also, indicating that CTOD during crack growth for a T-L specimen was 25% lower than for an L-T specimen.

Other authors indicate that the resistance to crack growth is much influenced by the materials microstructure such as the grain orientation and grain boundary. The same studies reported that crack growth rate was different even when the crack was subjected to the same loading parameter of continuum mechanics. The grain boundary acted as the barrier for propagation into adjacent grains [42].

A change in grain orientation in a rolled process is nominally equivalent to changing the fracture specimen orientation in a plate. It has been documented that fracture toughness and fatigue crack growth (FCG) rates differ with specimen orientation (that is L-T versus T-L) in plate products [43]. It was expected, since the alloy microconstituents were elongated in the rolling direction.

Studies performed in a nickel alloy (Inconel MA 754) under tensile hold cycles showed that specimens in longitudinal orientation suffered grain boundary damage and were fractured by transgranular initiation and intergranular crack propagation. In turn, long transverse orientation specimens exhibited reduced lives and the fracture mode was

intergranular crack initiation and propagation. Intergranular crack initiation and propagation occur at faster rates than transgranular cracking [44].

4.2 Methodology and experimental procedure

4.2.1 Aluminum alloy characteristics

The aluminum alloy 7075-T6 analyzed in this thesis has been widely used in the fabrication of airframe structures. This aluminum alloy contains zinc, magnesium, copper and chromium [45]. The T6 heat-treatment with the aging condition of the material provides high strength, but low fracture toughness at room and cryogenic temperatures and poor resistance to stress-corrosion cracking. Table 4.1 and Table 4.2 show the chemical composition limits and typical mechanical properties for AA7075-T6 alloy.

Table 4.1 AA7075-T6 chemical composition

Component	Min - Max wt%
Al	87.1 - 91.4
Cr	0.18 - 0.28
<u>Cu</u>	1.2 - 2.0
Fe	Max 0.5
<u>Mg</u>	2.1 - 2.9
Mn	Max 0.3
Other, each	Max 0.05
Other, total	Max 0.15
Si	Max 0.4
Ti	Max 0.2
Zn	5.1 - 6.1

Table 4.2 AA 7075-T6 alloy mechanical properties

Properties	Minimum
UTS (MPa)	537
Yield strength 0.2% offset (MPa)	505
Elongation (%)	11
Hardness HRB	87
Fracture Toughness K_{IC} (MPa · m ^{1/2})	27

The grain width corresponding to the longitudinal direction L in Figure 4.1 *a*) was estimated at $3.74 \pm 0.05 \mu\text{m}$ by AFM. It was not possible to determine the grain length since the grain boundaries could not be clearly revealed by etching. In Figure 4.1 *a*) grain size in longitudinal direction was determined using easyScan E-line[®] AFM. Figure 4.1 *b*) shows the zones in the sample and the grain orientation after etching using Keller's reagent. Keller's reagent was made up of w/w 5 HF concentrated, 0.75 HCl concentrated, 1.25 HNO₃ concentrated and 43.0 H₂O. Etching revealed a microstructure with elongated grain in the rolling direction.

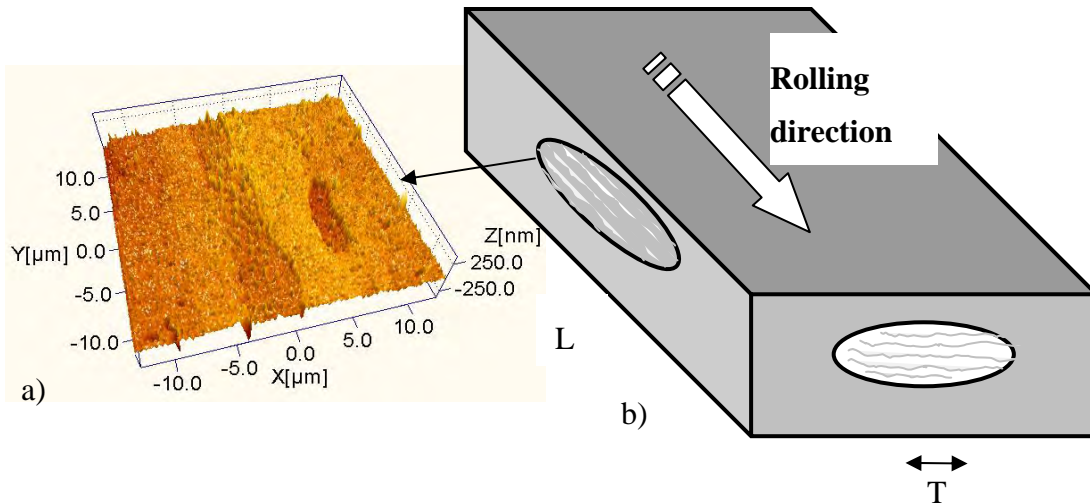


Figure 4.1 *a*) Image taken in contact mode with AFM at a longitudinal section parallel to the rolled surface revealing a microstructure characteristic of AA 7075-T6. *b*) Longitudinal and transversal grain orientation

4.2.2 Sample preparation and experimental fatigue testing

The AA 7075-T6 alloy was studied along two grain orientations, longitudinal and transversal to the plate, L and T respectively. Tension-tension fatigue tests were carried out in three point-bending on Charpy size specimens. Compact tension (CT), specimens 3.93 in (100 mm) x 0.78 in (20 mm.) x 0.19 in (5 mm.) were prepared. A vertical hydraulic MTS machine was employed in the fatigue – impact tests. All fatigue tests were run in air at room temperature under load control in tension-tension cycling with a sawtooth or triangular waveform at a frequency of 0.1 Hz, for 3880 cycles and an initial load of 1300 N.

After specimen failure, one side of the specimens was cut to observe the fracture in the AFM. A piece of the aluminum alloy was ground and polished, and then etched with Keller’s reagent to reveal and analyze the microstructure. Optical micrographs were taken to observe the fracture in the specimens according to grain orientation.

4.3 Results and Discussion

Figure 4.2 shows an irregular grain structure obtained as a result of solidification and plastic deformation. After rolling and thermal treatment, the solidification structure has disappeared and the grain size is function of other factors included T6 alloy thermal treatment.

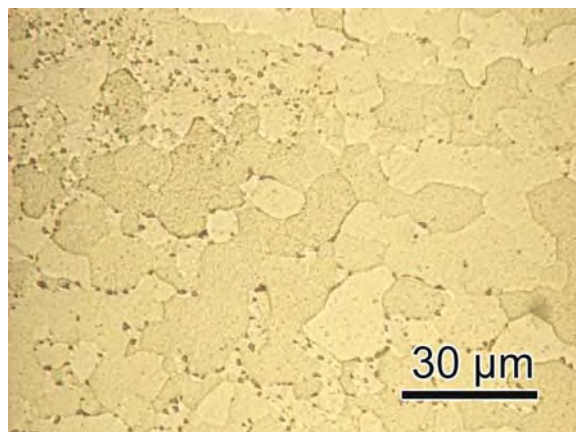


Figure 4.2 AA7075-T6 microstructure showing irregular grains

Figure 4.3 displays the grain structure and grain orientation along the longitudinal section parallel to the rolling surface of the specimen material plate.

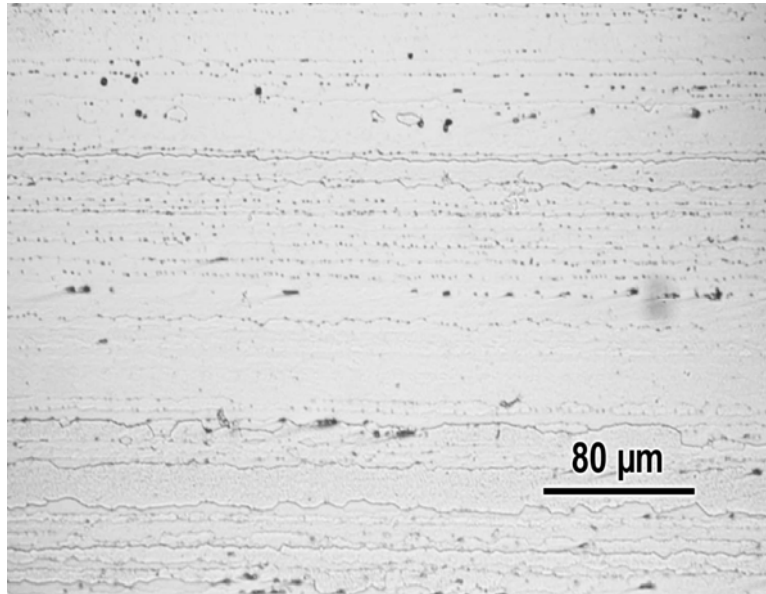


Figure 4.3 Optical micrograph of rolled sample revealing a microstructure characteristic of AA7075-T6 aluminum alloy

Figure 4.4 and Figure 4.5 correspond to the same image, presented in 2D and 3D. The grains oriented transversally (represented by T in Figure 4.1 b)) cover an area of $2519.5 \mu\text{m}^2$. AFM operating conditions were: static force used 20 nN, scanning frequency 2 Hz, and a scan range of $50 \mu\text{m}$ with $1.25 \mu\text{m}$ as z-range. Possibly, the crack growth occurs along a line of grain boundaries and therefore less energy was necessary for fast crack propagation. The fracture surface would be less rough than when we have a longitudinal orientation.

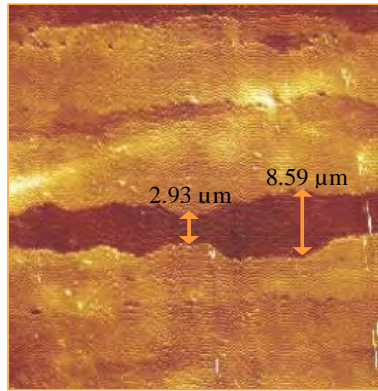


Figure 4.4 Transversal grain orientation in 2D, AFM image

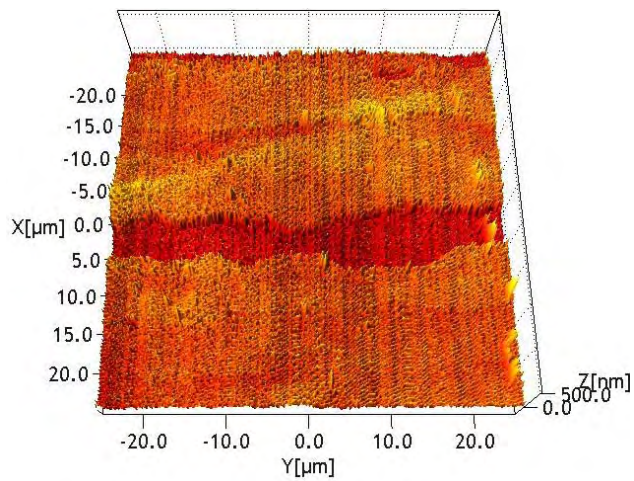


Figure 4.5 Transversal grain orientation in 3D, AFM image

The Figure 4.6 and Figure 4.8 show the crack growth difference between the transversal fracture surface and longitudinal one (indicated by the arrows).

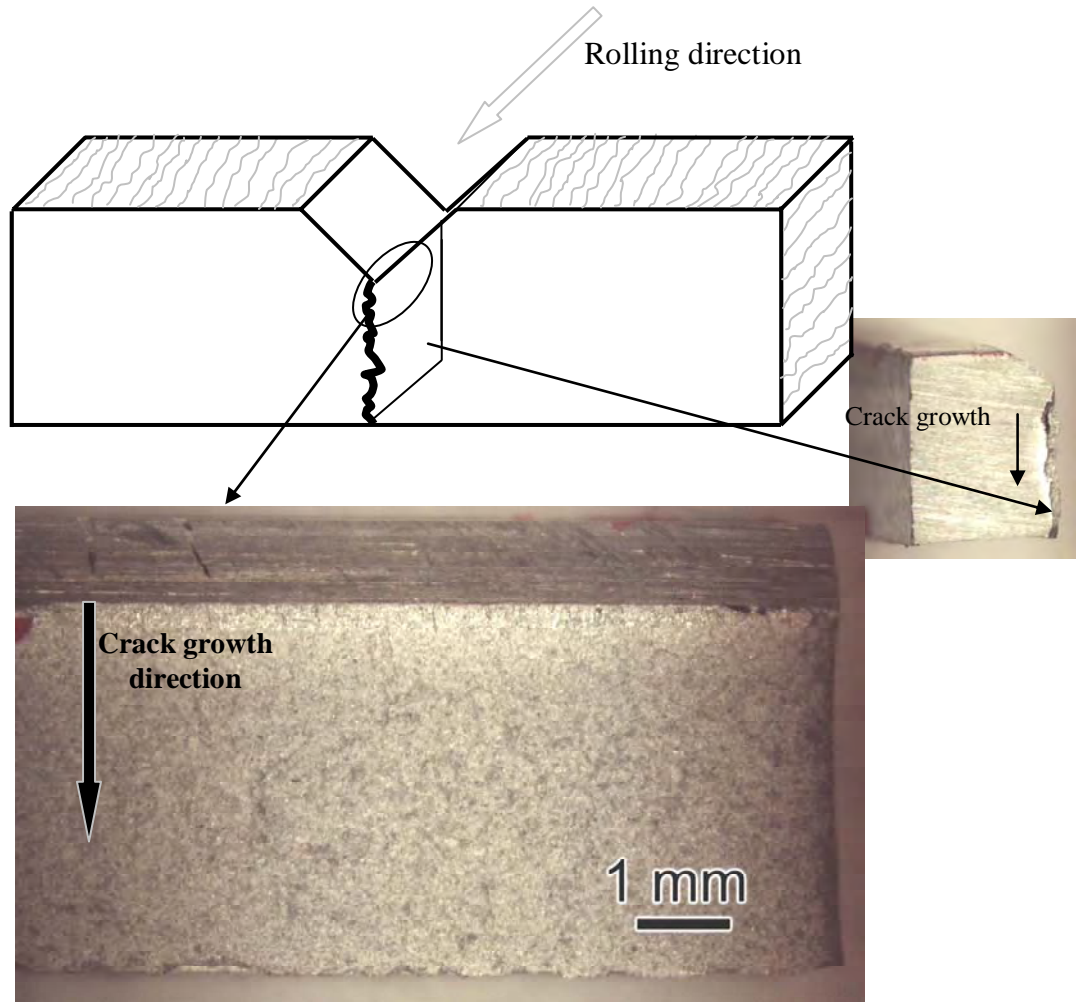


Figure 4.6 Transversal sample (T) after tested in fatigue-impact

The fracture along the T direction surface was smoother than L orientation. The fracture along the T orientation displays a bright zone in the crack initiation region as Figure 4.7 revealed. This zone began from the starting point of the crack to 0.25 mm along the growth direction (arrow indication in Figure 4.6). Several microcracks perpendicular to the crack front were distinguished in this area (Figure 4.7). The microcracks perpendicular at the grains orientation demonstrated a grain breaking along

of the front crack. A dark area at about 0.75 mm from the crack origin and growing in the width direction to final fracture is also noted.

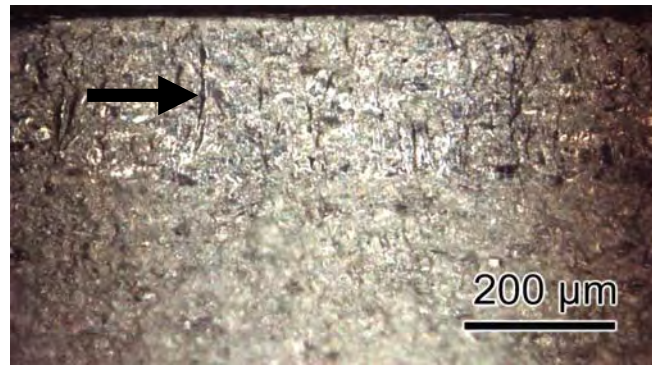


Figure 4.7 Microcracks perpendicular at crack growth direction (arrow point towards them)

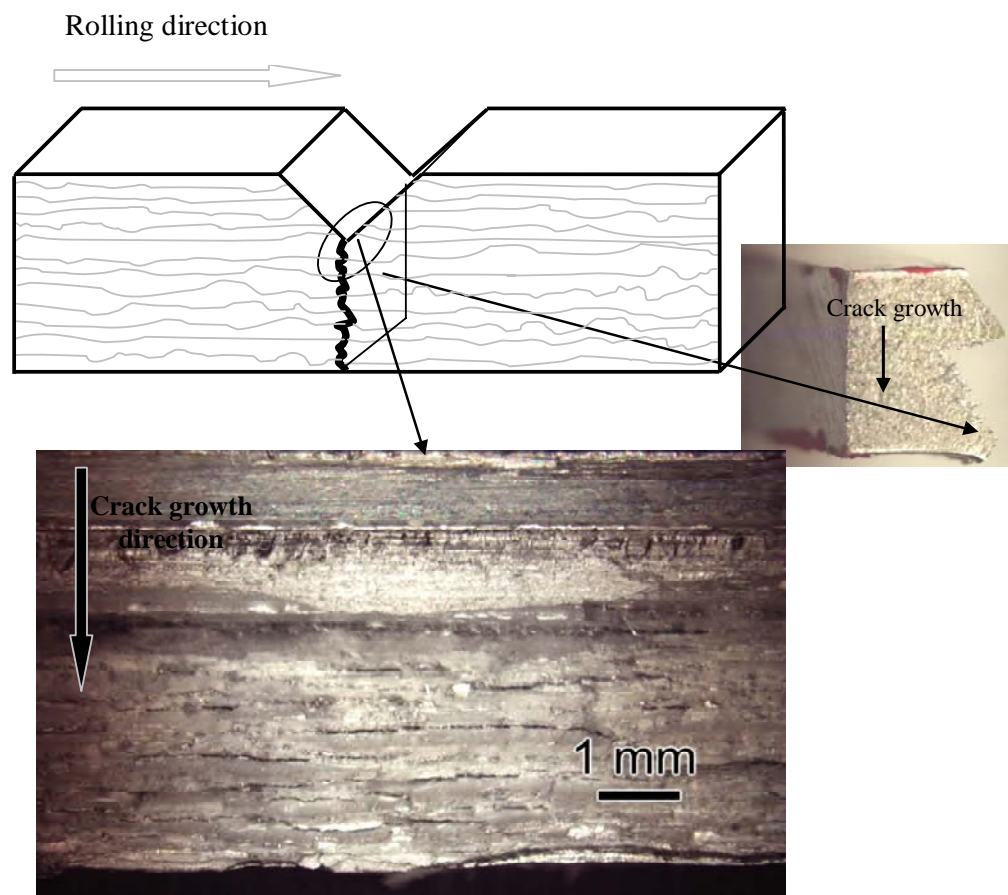


Figure 4.8 Longitudinal sample (L) after tested in fatigue-impact

Immediately after the initial region, a small zone exhibiting ductile fracture was apparent. This fracture type is similar to a cup-and-cone one since the regions between the splits resemble such as a tensile fracture (right photograph in Figure 4.8). Delaminations were observed along grain boundaries. Figure 4.8 illustrates this delaminations on longitudinal fatigued specimen.

According with the effect expected Figure 4.6 and Figure 4.8 evidence positively the great dependence fracture surface of aluminum 7075-T6 on the grain orientation. There was significant differences in fracture behavior for T and L cracks under mode I conditions. Under mode I type growth, crack in the T- orientation (along the rolling direction) results in a flat fracture, and crack in the L-orientation (perpendicular to the rolling direction) become an abrupt fracture. This was also observed by Amxtutz *et al.* [41]. Thus, the grain orientation does alter the crack growth process on the surface. With respect to grain orientation, two kinds of fracture behavior were presented in fatigued specimens: intergranular and transgranular fracture along the crack front.

In L-orientated sample (Figure 4.9), the crack path appears quite rough, with marked variations in crack trajectory. Perpendicular to the direction of nominal crack and for the T-orientation the crack path appears very straight and the fracture surface remained macroscopically flat during the entire fracture process. The T fracture surface displayed a typical dimpled rupture through the thickness and along the crack front. Figure 4.6 showed the fracture surface of AA7075-T6 in the L-orientation where delaminations were present across the thickness and parallel to the crack front. This differs from the growth in the T-orientation, where initially short cracks were present at 0.5 mm from the notch. These short cracks were present in the bright zone into the micrograph of the fracture surface of aluminum specimen (Figure 4.7).

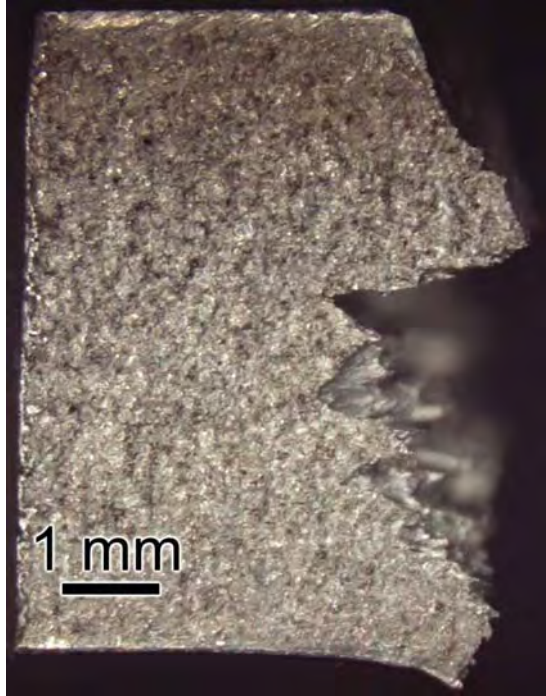


Figure 4.9 Irregular fracture in L orientation

On the other hand, the deformation associated with opening and closing of the crack produces a fracture surface with well-defined undulations which results in a striated appearance [46]. Along the first 20 microns from the crack origin in the crack growth direction, 7075-T6 aluminum alloy displays typical fatigue striations, shown in Figure 4.8. This pattern corresponds to the L orientation.

Fatigue striations shown in Figure 4.10, are perpendicularly to the crack propagation direction as the literature reported for aluminum alloys [47]. Striation width was determined by the fatigue stress and was of the order of 10^{-4} mm or less [27]. Figure 4.11 showed a profile along crack growth direction, where each striation was characterized by a peak and the distance between two connective peaks of these striations were revealed by SPIPTM software in the right corner. Among red and blue triangles the distance is 0.58707 μm and between clear green and dark green the distance was 0.78277 μm .

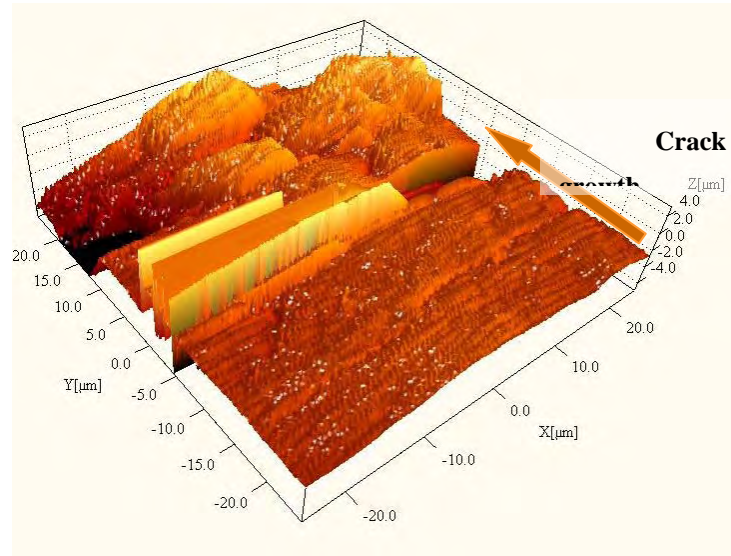


Figure 4.10 Fatigue striations on the fracture surface of AL7075-T6 in crack front direction

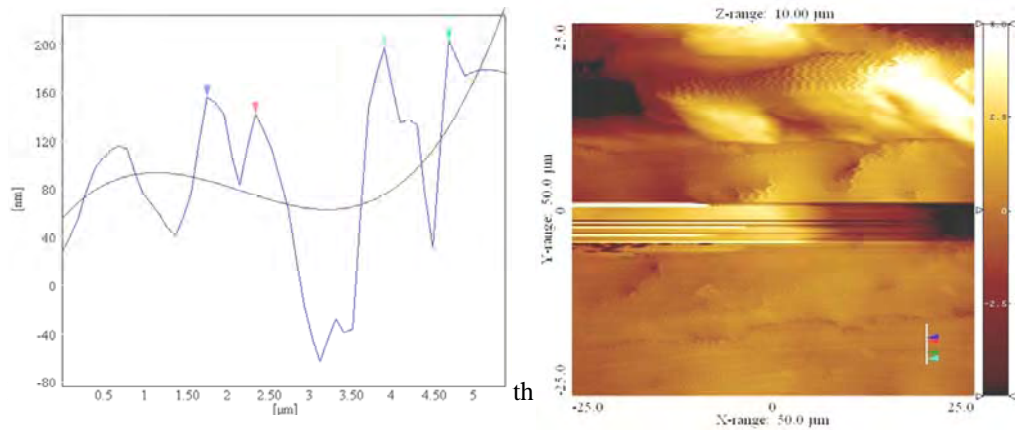


Figure 4.11 Striation profile in the crack growth direction

A flat fracture surface in T-orientation indicated that grains were elongated perpendicular to the rolling direction. They were parallel to the crack front and had a faster fracture than L-orientation. It is possible that this was developed since the fracture followed paths parallel to grain boundaries. Therefore, it is apparent that the crack growth did not encounter abrupt obstacles in the front crack.

The T-orientation aided at the fast crack growth as illustrated in the Figure 4.12. Contrary to the previous mechanism, following an L-orientation, the fracture occurred while grains were cut through along the crack front, which results in a rougher surface than T-orientation (Figure 4.13).

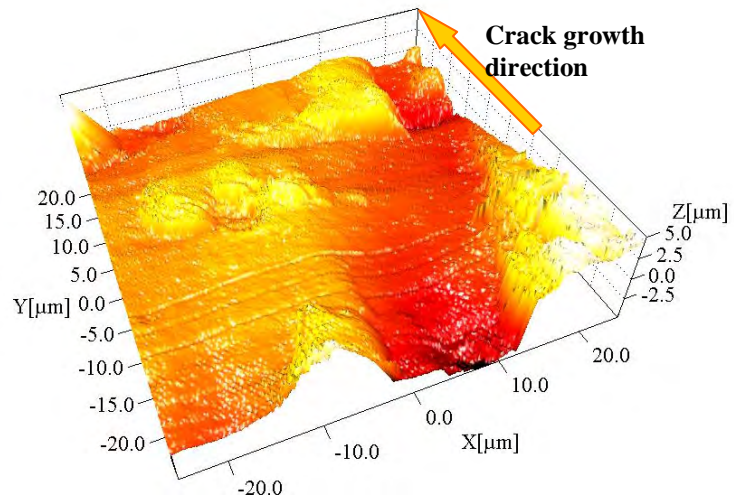


Figure 4.12 AA 7075-T6 grains showed in T-orientation

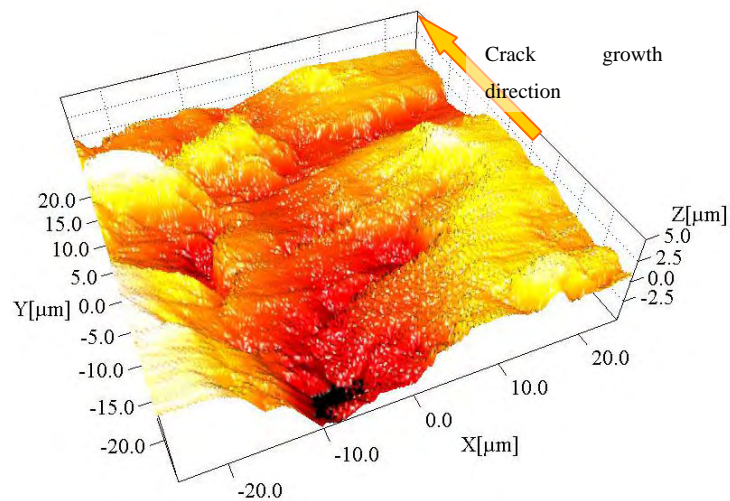


Figure 4.13 AA 7075-T6 grains showed in L-orientation

5 CONCLUSIONS

For the selected scan range (50 μm x 50 μm) and for the specimen conditions not all parameters were relevant to this type of fracture in the ultrahigh strength steel-AF1410, since they did not permit to correlate the crack growth parameters with the material roughness.

The results indicate that an explicit dependence of the roughness does not exist with the precrack line distance; rather a mean roughness is present along the sample.

The fractured surfaces obtained in the AF1410 steel had a self-affinity behavior since a qualitative indicator was present, i.e. Hurst exponent = 0.5.

The experimental configuration did not generate a clear change in the fracture surface formation process. For the selected scanning ranges and bandwidth parameters, a saturation regime was not reached in the six specimen conditions studied.

Oriented grain boundaries contained in AA 7075-T6 interacted with crack front conducting a large propagation rate in the transversal specimen, while the surface fractured was softer than longitudinal sample.

AFM analysis in the specimen fractured surface revealed a higher roughness in the hydrogen rich side than on the without hydrogen, corroborating the strong effect of hydrogen embrittlement on the input surface.

6 References

- [1]. Y. Nakai, T. Kusukawa, N. Hayashi. Scanning Atomic-Force Microscopy on Initiation and Growth Behavior of Fatigue Slip-Bands in α -brass. *Fatigue and Fracture Mechanics: 32*, ASTM STP 1406, R. Chon. American Society for Testing and Materials, West Conshocken, PA (2001) 122-135.
- [2]. K. Minoshima, Yoshitaka Oie, K. Komai. In Situ AFM imaging system for the environmentally induced damage under dynamic loads in a controlled environment. *ISIJ international* **43** (2003), number 4, 4.
- [3]. K. Komai, K. Minoshima, T. Miyawaki. Nanoscopic visualization of localized corrosion damage by means of atomic force microscope. Computational Mechanics Publications Southampton Boston, Kyoto University, Japan.
- [4]. K. Furukawa, Y. Murukami, S. Nishida. A method for determining stress ratio of fatigue loading from the width and height of striation. Elsevier Science Ltd. *Int. J. Fatigue* **20** No. 7 (1998) 509-516.
- [5]. S. Choi, H. Ishii, K. Tohgo. Cross Sectional Profiles and Dimensions of Fatigue Striations. *Journal of the Society of Materials Science, Japan.* **47** No. 8 August (1998) 852-857.
- [6]. T. S. Sriram, Chin-Ming Ke, Y. W. Chung. Fatigue deformation of silver single crystals: STM evidence for crack nucleation, measurements of slip irreversibility and verification of a new scaling relationship for fatigue life. Pergamon Press Ltd. **41** No. 8 August (1993) 2515-2521.
- [7]. P. Daguier, S. Henaux, E. Bouchaud, F. Creuzet. Quantitative analysis of a fracture surface by atomic force microscopy. Laboratoire CNRS/Saint-Gobain "Surface du verre et interfaces", France (1995).
- [8]. P. Daguier, E. Bouchaud. Fracture surfaces of complex metallic materials: roughness indices, scaling and universality. *La Revue de Métallurgie-CIT/Science et Génie des Matériaux*, France (1997).
- [9]. A. Saxea, F. Yang, L. Creteigny. Use of atomic force microscopy for studying fatigue crack initiation. Proceedings of the seventh international fatigue congress, 8-12 June, China. **4** (1999).
- [10]. Y. Tanaka, Y. Kagawa, Yu-Fu Liu, C. Masuda. Interface damage mechanism during high temperature fatigue test in SiC fiber-reinforced Ti alloy matrix composite. *Elsevier Materials Science and Engineering A314* (2001) 110-117.
- [11]. R. I. Stephens, A. Fatemi, R. R. Stephens, H. O. Fuchs. *Metal Fatigue in Engineering* 2nd edition. John Wiley & Sons, Inc, New York (2001).

- [12]. M. Hinojosa, E. Bouchaud, B. Nghiem. Rugosidad a larga distancia en superficies de fractura de materiales heterogéneos, Memorias del Congreso de la Materials Research Society, **539** (1999).
- [13]. R. Carpick page, Wisconsin University, Madison, WI. http://mandm.engr.wisc.edu/faculty_pages/carpick/research.htm
- [14]. A. L Barabási., H. E. Stanley. Fractal concepts in surface growth. Cambridge University press, Great Britain, 1995.
- [15]. R. Sum, P. Van Schendel. Operating instructions. Easy scan E-AFM (version 1.0) NanoSurf, Switzerland, 2003.
- [16]. <http://www.nanoscience.com/>
- [17]. C. K.Gupta. *Extractive Metallurgy of Molybdenum*, 1st ed., CRC Press, Inc., Boca Raton, Florida, 1992.
- [18]. R. P. Wei. Fracture toughness testing in alloy development, *Fracture toughness testing and its applications* ASTM **381**. (1964) 279-281.
- [19]. G. T. Murray. *Handbook of materials selection for engineering applications*, 1st ed., Marcel Dekker, Inc., New York, 159 1997.
- [20]. W. Callister Materials Science and Engineering an Introduction. Utah University, third edition, John Wiley & sons, Inc., USA, 1994.
- [21]. Humberto Raposo from Carpenter technology industry, under private communication.
- [22]. R. Jemian, 1990. Characterization of steels by anomalous small-angle x-ray scattering. Ph.D. Thesis. Northwestern University, Evanston, IL., 6 pp.
- [23]. K. Komai, K. Minoshima, T. Fujito. Influences of vibratory stresses on initiation of stress corrosion cracking in high-strength steel, Transactions of the Japan institute of metals, **27** No. 1(1986), 23.
- [24]. http://www.pacificnanotech.com/nano-roughness_single.html
- [25]. Atomic force microscopy for nano-surface texture/roughness. http://www.pacificnano.com/nano-roughness_surface-area-roughness-calculations.html
- [26]. Surface profile parameters. <http://www.predev.com/smg/parameters.htm>.
- [27]. N .Pérez. Fracture Mechanics, Department of Mechanical Engineering University of Puerto Rico, (2003).

- [28]. A. Quispitupa, B. Shafiq, M. Suárez, O. Uwakweh and N. Duque. Corrosion fatigue of high strength aircraft structural alloys, accepted for publication Journal of aircraft (2005).
- [29]. M. Zecchino. Characterizing surface quality why average roughness is not enough. Veeco Instruments, Inc. (2003). www.veeco.com/appnotes/AN511_Roughness.pdf
- [30]. M. Reyes Melo, S. Guerrero. Autoafinidad de superficies de fractura en materiales plásticos. Ingenierías, enero-marzo, **4** No. 1 (2001).
- [31]. J. Ramírez, 2004. Estudio estadístico de imágenes de AFM aplicado a películas delgadas magnéticas basadas en el sistema $\text{La}_{2/3}/\text{Ca}_{1/3}\text{MnO}_3$. Thesis. Universidad del Valle, Cali, Valle - Colombia.
- [32]. J. Aldaco Castañeda, M. Hinojosa Rivera. 2000 Autoafinidad de superficies de fractura en una aleación aluminio-silicio. Tesis M.S. Universidad Autónoma de Nuevo León, México.
- [33]. B.B. Mandelbrot, D.E. Passoja y A.J. Paullay, “Fractal Character of Fracture Surfaces of Metals”, Nature, 308, (1984), 721-722 pp.
- [34]. M. Hinojosa, E. Bouchaud, B. Nghiem. Rugosidad a larga distancia en superficies de fractura de materiales heterogéneos, Memorias del Congreso de la Materials Research Society, **539** (1999).
- [35]. M. Kutz. Mechanical engineer’s handbook, 2nd ed., John Wiley & Sons, Inc., printed in the United States of America, (1998).
- [36]. C. T. Sun. Mechanics of aircraft structures, John Wiley & Sons, Inc., printed in the United States of America, (1998).
- [37]. S. Charca, 2005. Study of hydrogen permeation and diffusion in steels: predictive model for determination for desorbed hydrogen concentration. M.S. Thesis. University of Puerto Rico, Mayagüez, PR, pp 14.
- [38]. C. Smith. Engineer to Win: The Essential Guide to Racing Car Materials Technology Or How to Build Winners.
- [39]. Handbook of manufacturing engineering. Edited by Jack M. Walker. USA (1996) 658.
- [40]. Fractography and Materials Science. Gilbertson/Zipp, editors. ASTM STP 733. American Society for Testing and Materials. USA (1983).
- [41]. B. E. Amxtutz, M. A. Sutton, D. S. Dawicke and M. L. Boone. Effects of mixed Mode I/II loading and grain orientation on crack initiation and stable tearing in 2024-T3 aluminum, Fatigue and fracture mechanics, ASTM STP 1296, R. S.

- Piasecik, J. C. Newman and N. E. Dowling, American Society for Testing and Materials, **27** (1997) 105-125.
- [42]. R. Wei and R. Gangloff, editors. Fracture mechanics. Perspectives and Directions, 12th symposium. ASTM STP 1020.
- [43]. R. Chona, editor. Fracture mechanics. 20th symposium. ASTM STP 1189 (1993).
- [44]. H. Solomon, G. Halford, L. Kaisand and B. Leis, editors. Low cycle fatigue. Symposium sponsored by ASTM Comitee E-9 (1988).
- [45]. R. D. Kane. Environmentally assisted cracking: predictive methods for risk assessment and evaluation of materials, equipment, and structures, printed in Philadelphia, PA, (2000).
- [46]. H. Derek. Fractography observing, measuring and interpreting fracture surface topography, Cambridge University Press, United Kingdom, (1999).
- [47]. ASM Handbook[®] Formerly Ninth edition, Metals Handbook, Fractography, **12**, pp 16 (1987).

APPENDIX

In the appendix has been shown the Matlab's program created to find the Hurst exponent in the AF1410 steel specimens. The figures represent the consecutive screens showed by the PC while the program runs.

```
% Imagen4.m

% Nairobi Duque

% FILENAME: Imagen4.m

% DATE: July 7, 2005

% VERSION: 01

%

clear all; close all;clc;

disp('*****')

disp('*          Imagen general          *')

disp('*          Diseno sin perfiles      *')

disp('*****')

%

%Pregunta para opcion de rotacion

%

disp('1)Rotar figura original 45°)

disp('2)Mantener figura original')

disp('*****')

disp('*PRESIONE UNA TECLA PARA CONTINUAR*')

disp('*****')

pause;
```

```

%
PRO = input('Ingrese su seleccion: ');
if isempty(PRO), break, end

PRO = round(PRO);
if (PRO<1) | (PRO>2)
    disp("")
    disp('No es una seleccion valida')
    disp("")
    disp('Presione una tecla para terminar ejecucion')
    pause;
end
if PRO == 1
    %Entradas
    m=input('Ingrese la distancia de barrido ');
    Q=input('Ingrese el nombre del archivo a cargar en formato NAMEFILE.asc
    ','s');
    L=load(Q);
    K=flipud(L);
    %Mide tamaño grid
    [oi ou]=size(K);
    % Vectores
    x=(m/oi):(m/oi):m;
    y=(m/oi):(m/oi):m;

```

```

%Figuras

figure (1),

surf(x,y,K),...

    title('Original surface'), xlabel('x (μm)'),...
    ylabel('y (μm)'), zlabel('z (μm)')

figure (2),

h = surf(x,y,K);

zdir = [0 0 1];

center = [0 0 0];

rotate(h,zdir,45,center)

title('Rotated surface'), xlabel('x (μm)'),...

    ylabel('y (μm)'), zlabel('z (μm)')

%%%%%%%%%%%%%%%%%%%%%%%%%%%%%%%%%%%%%%%%%%%%%%%%%%%%%%%%%%%%%%%%%%%%%%%%

%Calculo de perfiles

%%%%%%%%%%%%%%%%%%%%%%%%%%%%%%%%%%%%%%%%%%%%%%%%%%%%%%%%%%%%%%%%%%%%%%%%

%

%Reordenamiento de filas

R=flipud(K);

%Calculo de la diagonal

w=(oi/2);

ZX=zeros(w+1,w);

s=1;

r1=0;

% Grafica perfiles

```

```

for i=-w:2:w

    T=(diag(R,i))';

    [oq oz]=size(T);

    V=zeros(1,w);

    maximo=max(T);

    minimo=min(T);

    for j=1:1:w

        V(1,j)=T(1,(oz-w)/2+j);

    end

    V;

    ZX(s,:)=V;

    fq=(m/oi)*sqrt(2)*[0:1:w-1];

    r1=r1+(m/oi)*sqrt(2);

    s=s+1;

end

%%%%%%%%%%%%%%%%%%%%%%%%%%%%%%%%%%%%%%%%%%%%%%%%%%%%%%%%%%%%%%%%%%%%%%%%

%Calculo exponente rugosidad

%%%%%%%%%%%%%%%%%%%%%%%%%%%%%%%%%%%%%%%%%%%%%%%%%%%%%%%%%%%%%%%%%%%%%%%%

%

[yq yz]=size(fq);

B=zeros(yq,yz);

v=1;

for r=1:1:yz-1

    ZH=zeros(w+1,ceil((yz/r)-1));

```

```

[lq lz]=size(ZH);
for i=1:1:(w+1)
    for j=1:1:lz
        ZH(i,j)=abs(ZX(i,j*r+1)-ZX(i,j*r+1-r));
    end
end
N=mean(mean(ZH,2));
B(yq,v+1)=N;
v=v+1;
end
figure;
loglog(fq,B),...
    title('Promedio'), xlabel('r (μm)'),...
    ylabel('Zprom (μm)'),...
    grid on;
disp('*****')
disp(' *INGRESE EL PUNTO FINAL* ')
disp('*PRESIONE UNA TECLA PARA CONTINUAR*')
disp('*****')
pause;
AA=fq';
CC=B';
na=getfield(cursor_info,'DataIndex');
A=zeros(na,1);

```

```

C=zeros(na,1);

for i=1:1:na
    A(i,1)=AA(i,1);
    C(i,1)=CC(i,1);
end

g = fitype('a*x^b');
coef=fit(A,C,g)
figure;
loglog(A',C'),...
    title('Pendiente'), xlabel('r (μm)'),...
    ylabel('Zprom (μm)'),...
    grid on;
elseif PRO==2
    %Entradas
    m=input('Ingrese la distancia de barrido ');
    Q=input('Ingrese el nombre del archivo a cargar en formato NAMEFILE.asc
', 's');

L=load(Q);
K=flipud(L);
%Mide tamaño grid
[oi ou]=size(K);
% Vectores
x=(m/oi):(m/oi):m;
y=(m/oi):(m/oi):m;

```

```

%Figuras

figure (1),

surf(x,y,K),...

    title('Original surface'), xlabel('x (μm)'),...
    ylabel('y (μm)'), zlabel('z (μm)')

%%%%%%%%%%%%

%Calculo de perfiles

%%%%%%%%%%%%

%

s=1;

r1=0;

%Grafica perfiles

for i=1:1:oi

    V=zeros(1,oi);

    for j=1:1:oi

        V(1,j)=K(i,j);

    end

    V;

    maximo=max(V);

    minimo=min(V);

    ZX(s,:)=V;

    fq=(m/oi)*[0:1:oi-1];

    r1=r1+(m/oi);

    s=s+1;

```

```

end

%%%%%%%%%%%%%%%%%%%%%%%%%%%%%%%%%%%%%%%%%%%%%%%%%%%%%%%%%%%%%%%%%%%%%%%%

%Calculo exponente rugosidad

%%%%%%%%%%%%%%%%%%%%%%%%%%%%%%%%%%%%%%%%%%%%%%%%%%%%%%%%%%%%%%%%%%%%%%%%

%

[yq yz]=size(fq);

B=zeros(yq,yz);

v=1;

for r=1:1:yz-1

    ZH=zeros(oi,ceil((yz/r)-1));

    [lq lz]=size(ZH);

    for i=1:1:oi

        for j=1:1:lz

            ZH(i,j)=abs(ZX(i,j*r+1)-ZX(i,j*r+1-r));

        end

    end

end

N=mean(mean(ZH,2));

B(yq,v+1)=N;

v=v+1;

end

figure;

loglog(fq,B),...

    title('Promedio'), xlabel('r (μm)'),...

    ylabel('Zprom (μm)'),...

```

```

    grid on;

disp('*****')

disp(' *INGRESE EL PUNTO FINAL* ')

disp('*PRESIONE UNA TECLA PARA CONTINUAR*')

disp('*****')

pause;

AA=fq';

CC=B';

na=getfield(cursor_info,'DataIndex');

A=zeros(na,1);

C=zeros(na,1);

for i=1:1:na

    A(i,1)=AA(i,1);

    C(i,1)=CC(i,1);

end

g = fitype('a*x^b');

coef=fit(A,C,g)

figure;

loglog(A',C),...

    title('Pendiente'), xlabel('r (µm)'),...

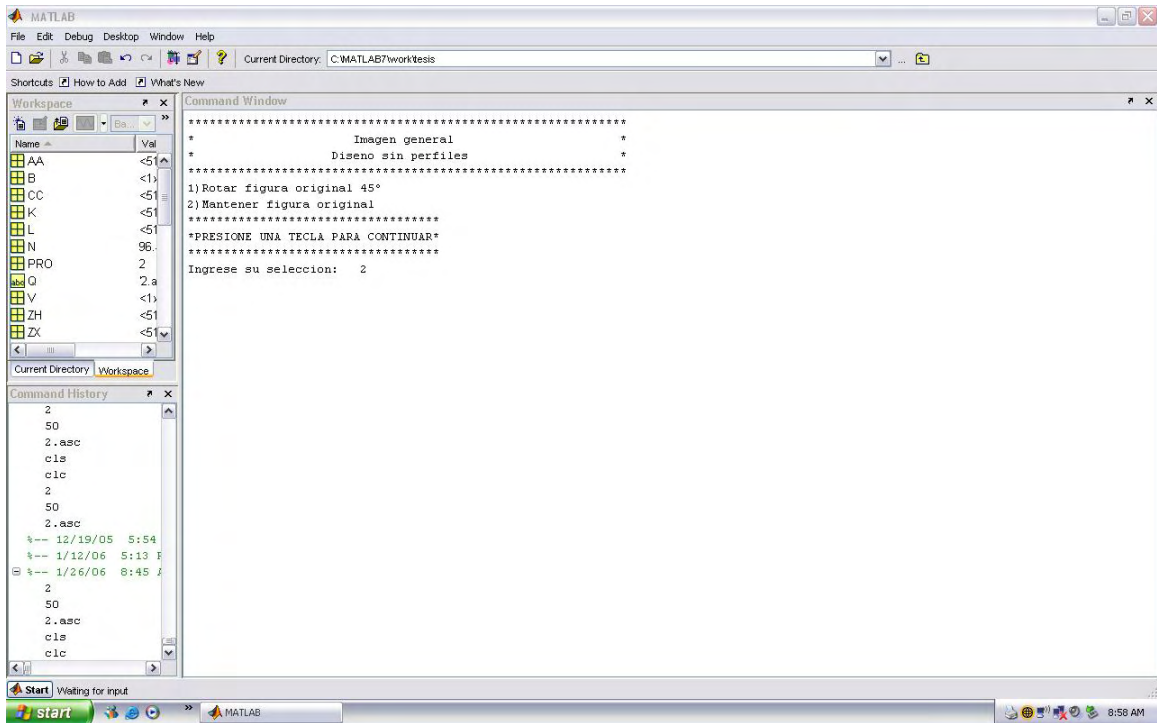
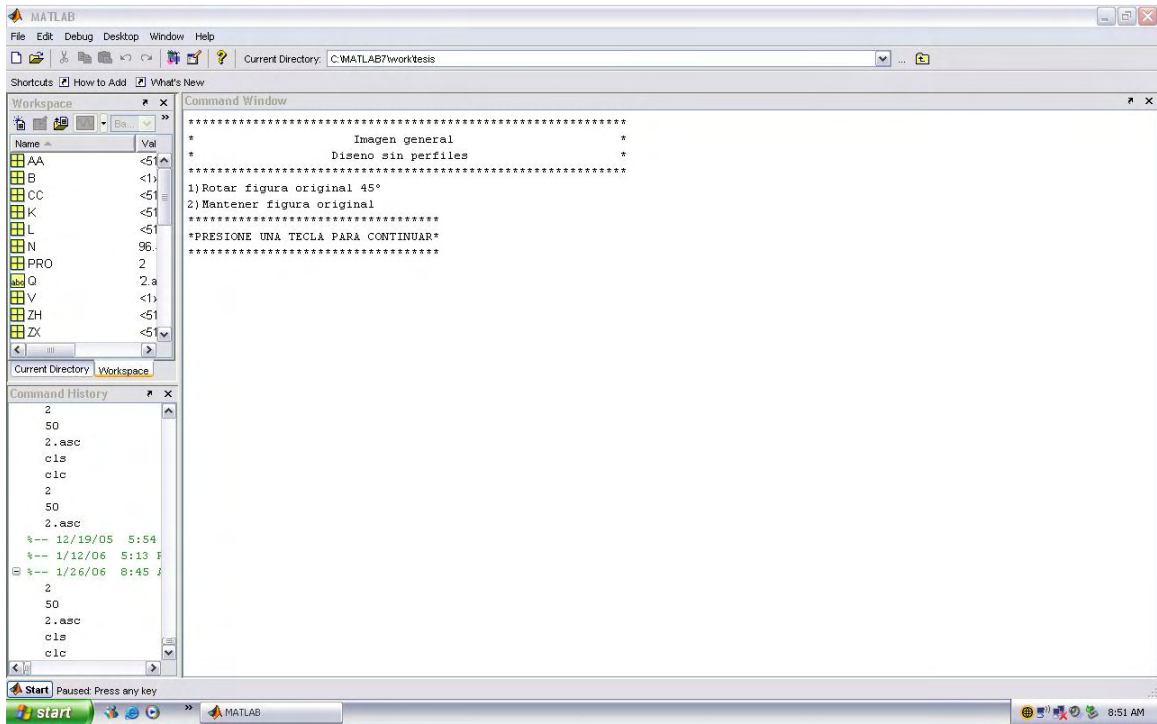
    ylabel('Zprom (µm)'),...

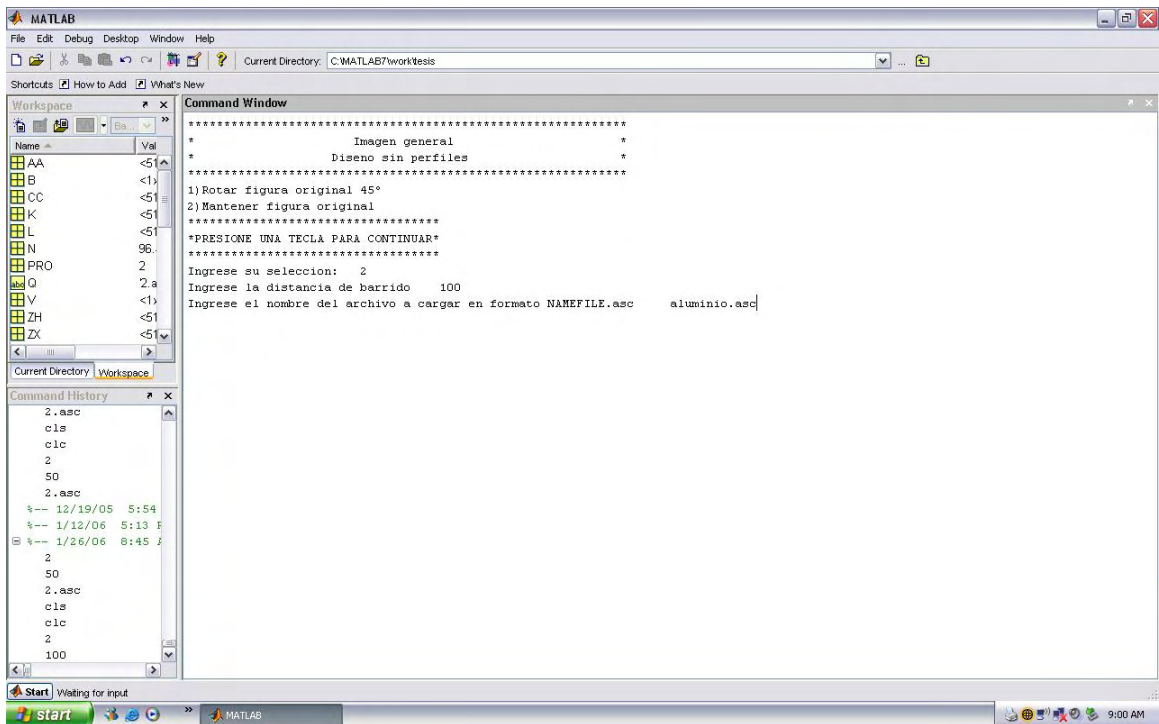
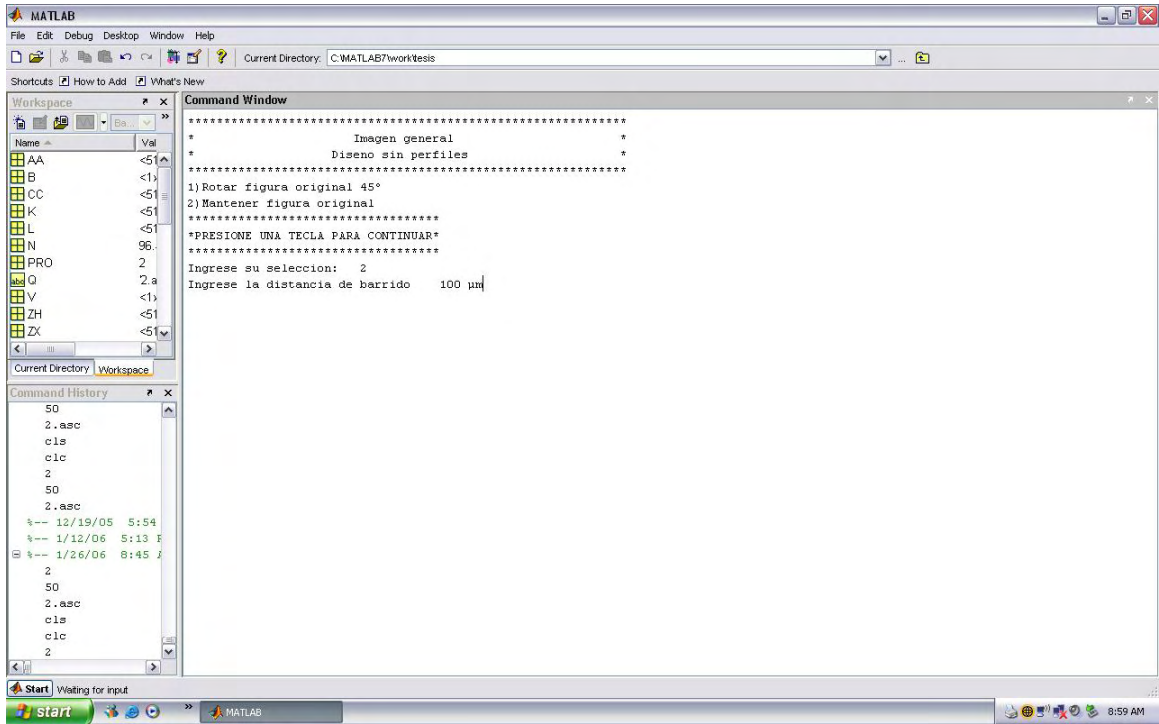
    grid on;

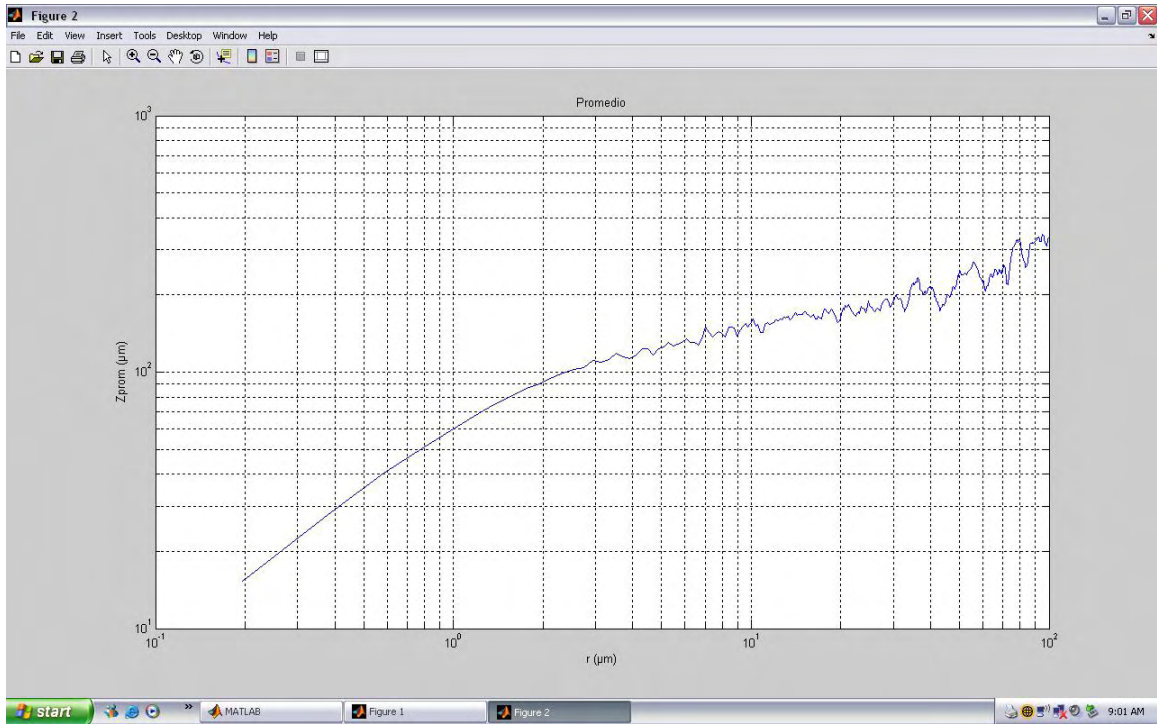
break

end % if PRO

```







MATLAB Command Window output:

```

*****
*          Imagen general          *
*          Diseño sin perfiles     *
*****
1)Rotar figura original 45°
2)Mantener figura original
*****
*PRESIONE UNA TECLA PARA CONTINUAR*
*****
Ingrese su seleccion: 2
Ingrese la distancia de barrido   100
Ingrese el nombre del archivo a cargar en formato NAMEFILE.asc   aluminio.asc
*****
*INGRESE EL PUNTO FINAL*
*PRESIONE UNA TECLA PARA CONTINUAR*
*****

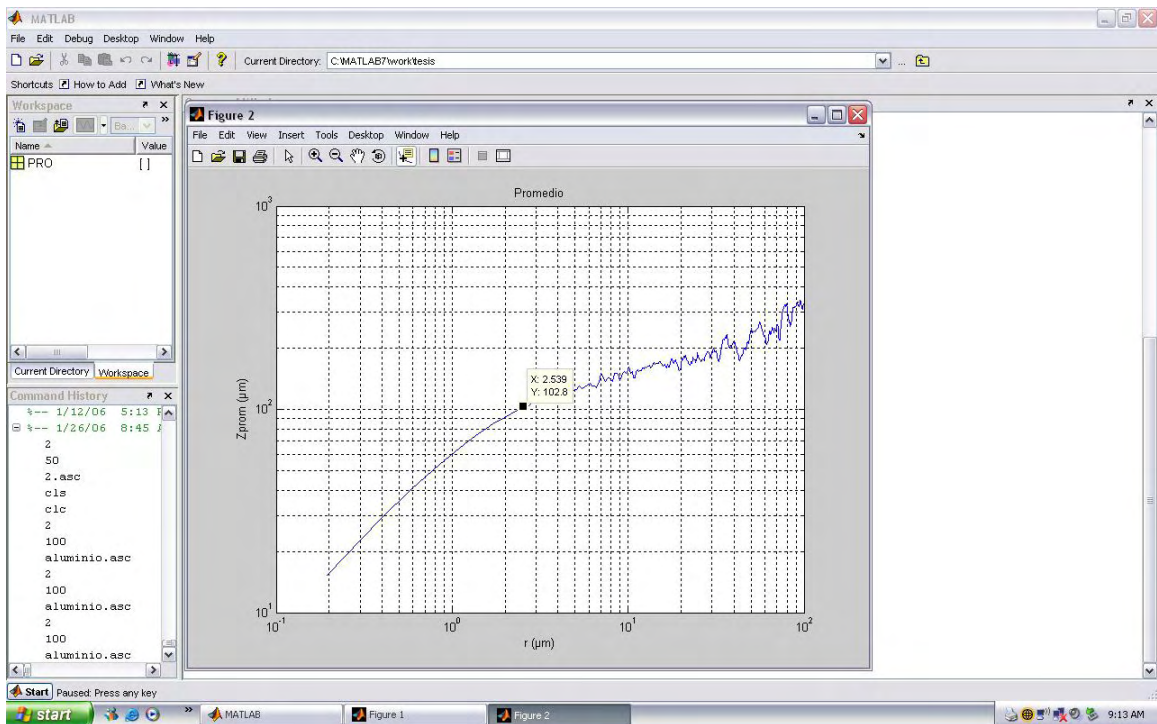
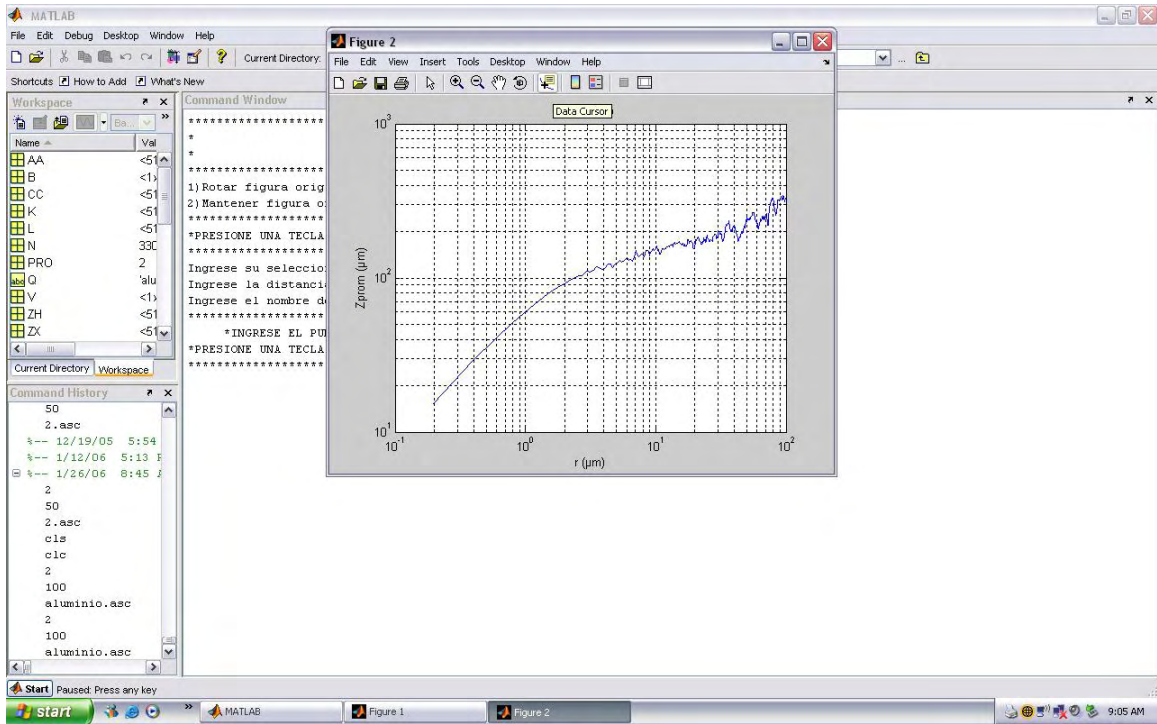
```

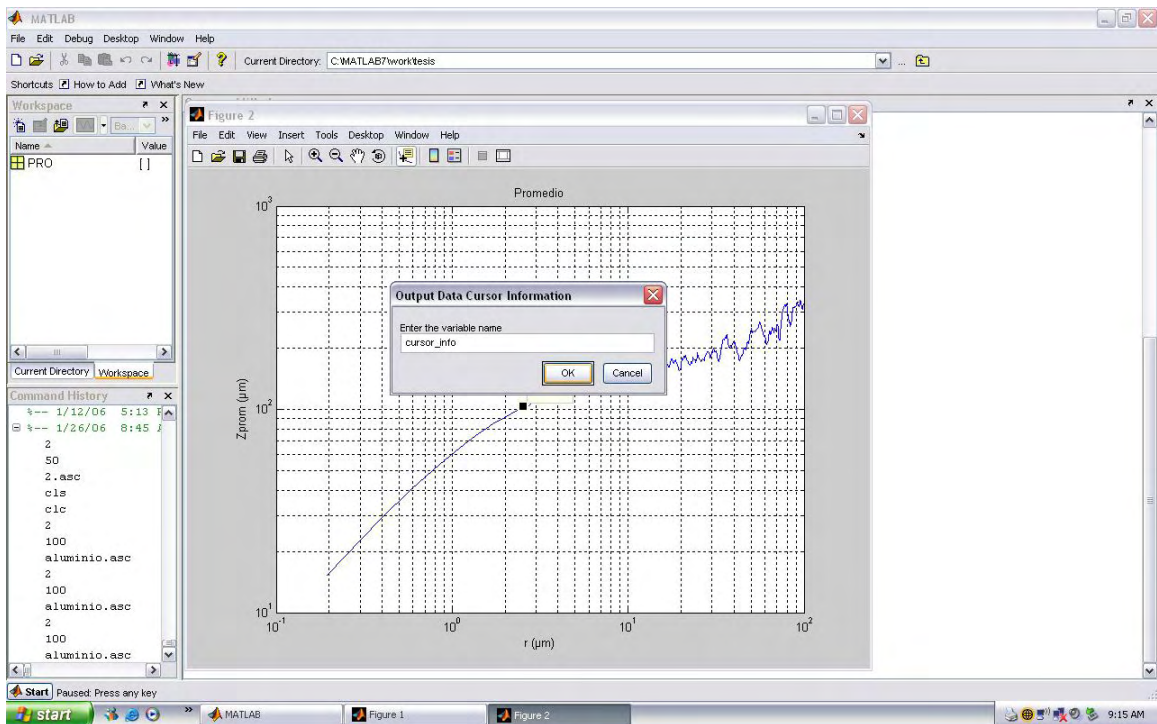
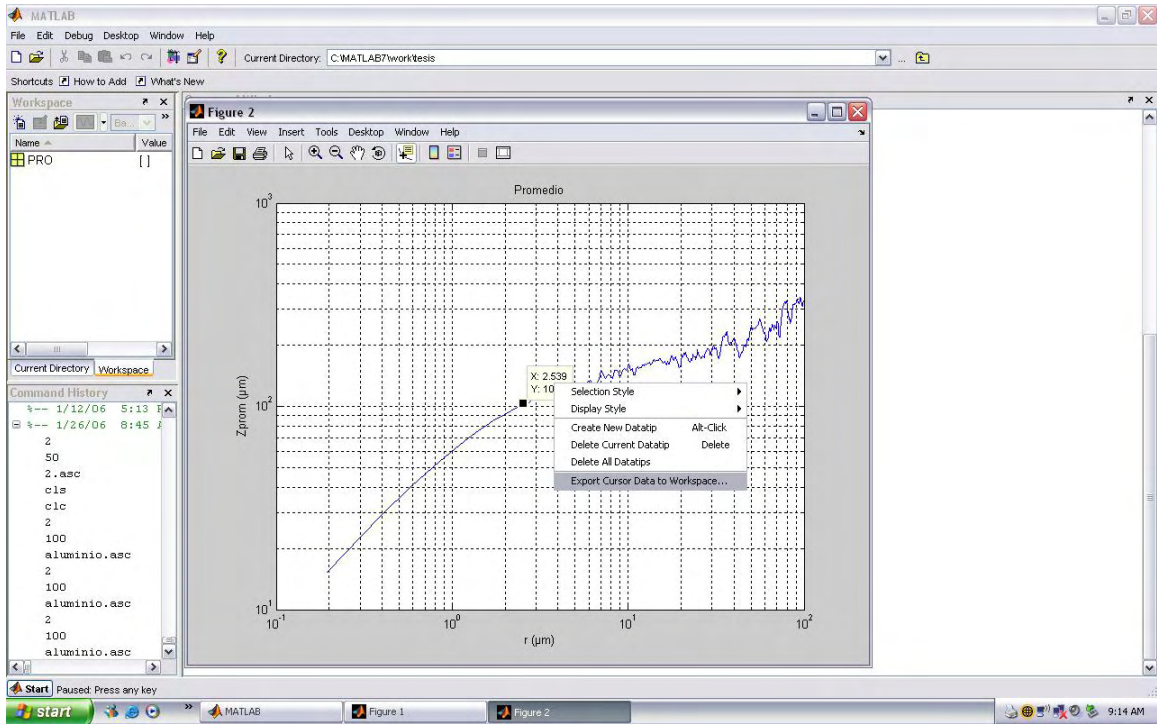
Command History:

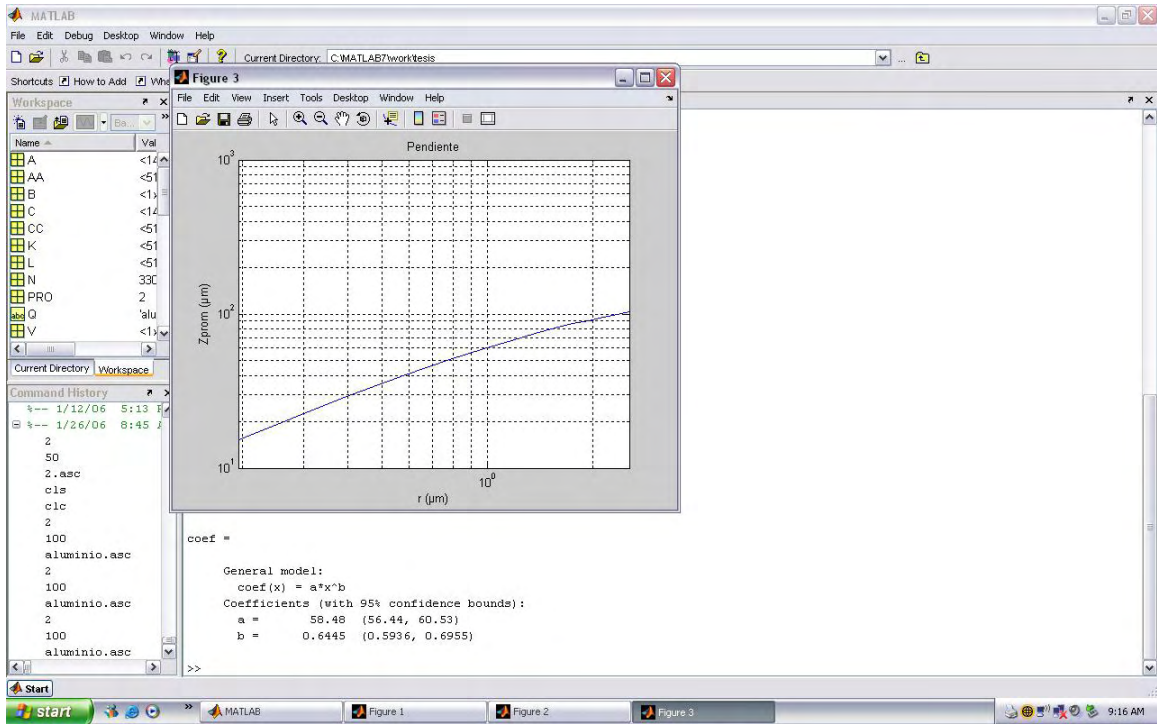
```

c1e
c1c
2
50
2.asc
12/19/05 5:54
1/12/06 5:13
1/26/06 8:45
2
50
2.asc
c1e
c1c
2
100
aluminio.asc

```







```

Editor - C:\MATLAB7\work\tesis\aluminio.asc
File Edit Text Cell Tools Debug Desktop Window Help
171 -1.36986 -2.05345 -2.73705 -2.73973 -2.73973 -2.73973 -2.73973 -2.06418 -1.38059 -1.36986 -1.36986 -0.601119 0.163001
478 -0.195695 -0.146867 -0.0980388 -0.146484 -0.195312 -0.14725 -0.0984218 -0.0978474 -0.0978474 -0.0978474 -0.0978474 1.29321 2.7121 2.74
479 -3.13112 -2.34987 -1.56862 -2.34374 -3.12499 -2.356 -1.57475 -1.56556 -1.56556 -1.56556 -1.56556 -0.892554 -0.206091
480 -5.69817 -4.27641 -2.85466 -4.26524 -5.68702 -4.28757 -2.86581 -2.84908 -2.84908 -2.84908 -2.84908 -2.80403 -2.75807
481 -2.76275 -2.07341 -1.38408 -2.06801 -2.75734 -2.07882 -1.38948 -1.38137 -1.38137 -1.38137 -1.38137 -0.618262 0.160113
482 0 0 0 0.0429145 0.085998 0.0435903 0.000506862 0 0 0 0 1.39669 2.82132 1.46373 0.0391074 0.0419008 0.0849843 1.46627 2.8909
483 0 0 0 0.772461 1.54796 0.784626 0.00912352 0 0 0 0 0.678635 1.37084 0.71121 0.0190018 0.754214 1.52972 2.22454 2.91675 2.94
484 -0.0805802 -0.0805802 -0.0805802 1.34132 2.76682 1.36371 -0.0637861 -0.0805802 -0.0805802 -0.0805802 -0.0805802 -0.0805802 -0.0805802
485 -1.54829 -1.54829 -1.54829 -0.855936 -0.160856 -0.845033 -1.54011 -1.54829 -1.54829 -1.54829 -1.54829 -1.54829 -1.54829
486 -2.86635 -2.86635 -2.86635 -2.86635 -2.86635 -2.86635 -2.86635 -2.86635 -2.86635 -2.86635 -2.86635 -2.86635 -2.86635
487 -1.39864 -1.39864 -1.39864 -1.39864 -1.39864 -1.39864 -1.39864 -1.39864 -1.39864 -1.39864 -1.39864 -1.39864 -1.39864
488 0.0690687 0.0690687 0.0690687 0.0690687 0.0690687 0.0690687 0.0690687 0.0690687 0.0690687 0.0690687 0.0690687 0.102295 0.137462 0.138137 0.138137
489 1.53678 1.53678 1.53678 1.53678 1.53678 1.53678 1.53678 1.53678 1.53678 1.53678 1.53678 1.53678 1.53678 1.53678 1.53678 1.53678 1.53678 1.53678 1.53678
490 2.87786 2.87786 2.87786 2.87786 2.87786 2.87786 2.87786 2.87786 2.87786 2.87786 2.87786 2.87786 2.87786 2.87786 2.87786 2.87786 2.87786 2.87786 2.87786
491 1.41015 1.41015 1.41015 1.41015 1.41015 1.41015 1.41015 1.41015 1.41015 1.41015 1.41015 1.41015 1.41015 1.41015 1.41015 1.41015 1.41015 1.41015 1.41015
492 0 0.0287223 0.0574446 0.0289476 0.000225272 0 0 0 0 1.41642 2.8554 2.91178 2.9405 2.94118 2.94118 1.51376 0.0460458 0 0 0
493 0 0.671141 1.52228 0.767111 0.00596971 0 0 0 0 0.695486 1.40205 2.16213 2.92327 2.94118 2.94118 1.51376 0.0460458 0 0 0
494 0.103603 1.54546 2.98732 1.55677 0.114912 0.103603 0.103603 0.103603 0.103603 0.103603 0.103603 0.103603 0.103603 0.103603 0.103603 0.103603 0.103603 0.103603 0.103603
495 3.03902 3.74847 4.45791 3.75403 3.04459 3.03902 3.03902 3.03902 3.03902 3.03902 3.03902 3.03902 3.03902 3.03902 3.03902 3.03902 3.03902 3.03902 3.03902
496 5.83631 5.83631 5.83631 5.83631 5.83631 5.83631 5.83631 5.83631 5.83631 5.83631 5.83631 5.83631 5.83631 5.83631 5.83631 5.83631 5.83631 5.83631 5.83631
497 4.3686 4.3686 4.3686 5.12103 5.87643 5.88235 5.88235 5.13584 4.38045 4.3686 4.3686 4.3686 4.3686 4.3686 4.3686 4.3686 4.3686 4.3686 4.3686
498 2.90089 2.92099 2.9411 4.3831 5.83071 5.86201 5.88212 4.45178 3.00417 2.96168 2.94157 1.52196 0.0743514 1.45383 2.90144 2.94118 2.94118 2.94118 2.94118
499 1.43318 2.1857 2.93823 3.65356 4.36874 5.12098 5.87935 5.17558 4.4604 3.70846 2.95599 2.24001 1.52483 2.20636 2.92154 2.94118 2.94118 2.94118 2.94118
500 0.0690687 1.51955 2.97002 2.97571 2.97571 4.41481 5.86529 5.88235 5.88235 4.47159 3.03935 3.01025 3.01025 3.01025 3.01025 2.99348 2.97625 2.97571 2.97
501 3.00449 3.72255 4.44061 4.44342 4.44342 5.15585 5.87391 5.88235 5.88235 5.91345 5.94505 5.94567 5.94567 5.94567 5.94567 5.21659 4.46694 4.44342 4.44342
502 5.88235 5.88235 5.88235 5.86805 5.85369 5.85357 5.85357 5.85357 5.85357 5.85357 5.85357 5.85357 5.85357 5.85357 5.85357 5.85357 5.85357 5.85357 5.85357
503 5.88235 5.88235 5.88235 5.1385 4.39172 4.38586 4.38586 4.38586 4.38586 5.83055 7.29826 7.32704 7.32704 7.32704 7.32704 6.6259 5.90497 5.159 4.41222
504 5.85933 5.87082 5.88231 4.204 2.95269 2.92978 2.91829 2.92951 2.941 4.37456 5.83078 5.85933 5.85933 5.85933 5.85933 5.85933 5.85933 5.85933 5.85933
505 4.39162 5.13553 5.87944 4.204 2.95269 2.2031 1.4592 2.1856 2.92951 3.65363 4.37743 4.39162 4.39162 4.39162 4.39162 4.39162 4.39162 4.39162 4.39162
506 2.95844 4.41754 5.87663 4.204 2.95269 1.49353 0.0344329 1.4592 2.91829 2.94118 2.94118 2.94118 2.94118 2.94118 2.94118 2.94118 2.94118 2.94118 2.94118
507 4.42615 5.15283 5.8795 4.204 2.95269 2.2202 1.49353 2.2031 2.92978 2.94118 2.94118 2.94118 2.94118 2.94118 2.94118 2.94118 2.94118 2.94118 2.94118
508 5.88235 5.88235 5.88235 4.204 2.95269 2.94118 2.94118 2.94685 2.9526 2.94703 2.94129 4.38011 5.84782 5.88235 5.88235 4.6052 2.99855 2.94712 2.94138
509 5.88235 5.88235 5.88235 4.204 2.95269 2.94118 2.94118 3.67066 4.40882 3.69381 2.95565 4.38011 5.84782 5.88235 5.88235 5.17283 4.44329 3.70539 2.96723
510 5.88235 5.87948 5.87661 4.4175 2.95267 2.94118 2.94118 4.39162 5.85933 4.44049 2.97565 4.38305 5.84789 5.88235 5.88235 5.87956 5.87669 4.45771 2.99288
511 5.88235 5.14706 4.41177 3.67934 2.94692 2.94118 2.94118 4.39162 5.85933 5.16142 4.429 5.1327 5.86512 5.88235 5.88235 5.16725 4.43195 3.69945 2.96703
512 5.88235 4.41464 2.94693 2.94118 2.94118 2.94118 2.94118 4.39162 5.85933 5.88235 5.88235 5.88235 5.88235 5.88235 5.88235 5.88235 4.45493 2.98722 2.94118 2.94118
513
  
```